A posteriori error estimation for isogeometric analysis using the concept of Constitutive Relation Error

Phuong Thai, Ludovic Chamoin, Cuong Ha-Minh

To cite this version:

Phuong Thai, Ludovic Chamoin, Cuong Ha-Minh. A posteriori error estimation for isogeometric analysis using the concept of Constitutive Relation Error. Computer Methods in Applied Mechanics and Engineering, 2019, 355, pp.1062-1096. 10.1016/j.cma.2019.05.021 . hal-02155081

HAL Id: hal-02155081
https://hal.science/hal-02155081

Submitted on 25 Oct 2021

Version of Record: https://www.sciencedirect.com/science/article/pii/S0045782519302919
Manuscript_dc7a3c172dfde4143d5ec44f969ccc4c

A posteriori error estimation for isogeometric analysis using the concept of Constitutive Relation Error

H.P. Thai[a], L. Chamoin[a,*], C. Ha-Minh[a]

[a]*LMT, ENS Cachan, CNRS, Université Paris Saclay*
61 Avenue du Président Wilson, 94235 Cachan, France

Abstract

The paper deals with the Isogeometric Analysis (IGA) technology, which has received much attention over the last decade due to its increased flexibility, accuracy, and robustness in many engineering simulations compared to classical Finite Element Analysis (FEA). In this context, we present a verification method, based on duality and the concept of Constitutive Relation Error (CRE), that enables to derive fully computable *a posteriori* error estimates on the numerical solution provided by IGA. Such estimates, which can be used for a wide class of structural mechanics models, thus constitute effective and practical tools to quantitatively control the numerical accuracy and drive adaptive algorithms. The focus is here on the construction of so-called admissible flux fields which is a key ingredient of the CRE concept, and which was until now almost exclusively addressed in the FEA framework alone. We show that this construction can be performed in a similar way for FEA and IGA, provided some technical issues (due to the use of B-Spline/NURBS basis functions instead of Lagrange polynomials) are carefully addressed. We also use the CRE concept along with adjoint techniques and local enrichments in order to derive accurate goal-oriented error estimates. Two- and three-dimensional numerical experiments are presented, for thermal, linear elasticity and nonlinear damage problems, to illustrate the capabilities and versatility of the proposed approach.

Keywords: Isogeometric analysis, Model verification, A posteriori error estimation, Constitutive relation error, Duality

---

1. Introduction

Performing numerical simulations from complex models based on partial differential equations has now become a common practice in engineering activities. Focusing on structural mechanics applications, a classical framework to address such simulations is the finite element method leading to the so-called Finite Element Analysis (FEA). However, a major

---

[*] Corresponding author

Email addresses: `hpthai@lmt.ens-cachan.fr` (H.P. Thai), `chamoin@lmt.ens-cachan.fr` (L. Chamoin), `cuong.ha-minh@lmt.ens-cachan.fr` (C. Ha-Minh)

Preprint submitted to Computer Methods In Applied Mechanics and Engineering *May 2, 2019*

drawback and practical issue of FEA is that it intrinsically suffers from a complex link with Computer-Aided-Design (CAD) softwares which are employed to generate and design the geometry of mechanical structures. On the one hand, the geometry representation which is involved in FEA is based on piecewise low-order polynomial functions (i.e. Lagrange polynomials, supported by polygonal meshes); it is dictated by the finite dimensional subspace considered to compute an approximate solution of the problem. On the other hand, the exact structural geometry generated by CAD is classically built from splines or NURBS (Non Uniform Rational B-Splines) functions which are smooth functions that enable to represent complex objects. Due to this difference in the geometry representation, the transfer from a CAD model to a FEA model requires powerful mesh generation tools and is in practice a very time-consuming process. In addition, when dealing with the approximate solution itself, it is well-known that low-order FEA requires a very fine mesh size to produce accurate results in high gradients regions (e.g. in the case of singular solution with stress concentration phenomena) whereas high-order FEA has some restrictions on element topologies and continuity, so that it is hardly implemented in commercial FEA software.
After pioneering attempts [48, 43] to foster the link between CAD and FEA, and therefore facilitate numerical simulations with domains generated by CAD, a general computational framework proposing a direct link and referred to as Isogeometric Analysis (IGA) was introduced in [45, 23]. The idea consists of constructing the approximation basis, still using a standard isoparametric formulation, from the B-Spline or NURBS functions representing the CAD geometry. IGA thus aims at directly using the CAD representation of the geometry in the analysis step. It enables the simple use of smooth functions with high-order continuity (compared with C^0-continuity associated with Lagrange polynomials), so that fewer dofs are necessary compared to FEA to represent solutions of PDEs with high-order derivatives. Furthermore, it simplifies mesh refinement as the geometry is represented exactly at the lowest level of discretization and is unchanged throughout the refinement process, so that no further communication with CAD is required. IGA was thoroughly studied and analyzed in the last decade [7, 33, 46, 63, 9, 4, 76], and its potential was demonstrated by successful applications to a wide range of structural mechanics problems [22, 8, 31, 41, 84, 49, 10, 14, 63, 80, 25, 12, 67, 27, 44, 51, 30]. Extensive numerical studies showed that beyond the reinforced link between CAD and analysis, IGA was a powerful computational mechanics technology bringing both accuracy and robustness. Furthermore, it was shown that the IGA concept could be easily incorporated into existing FE codes by using the Bezier extraction [11, 77]. Several open source IGA codes are available nowadays, such as PetIGA [24], and IGA implementations in commercial simulation software exist such as in Abaqus or LS-Dyna. Let us also quote a related method, proposed in [79] and denoted NURBS enhanced FEM (NEFEM), that involves NURBS functions to construct the boundary of the mechanical structure alone while the interior remains discretized using FEA Lagrange basis functions.

Despite its performance, and as for any numerical method, IGA is associated with discretization error that needs to be effectively assessed to control the quality of the approximation and drive automated adaptive procedures. This verification step is a crucial engineering topic as the massive use of virtual prototyping, with possibly very complex models, relies on the capacity to warrant the relevance of the numerical solutions usually obtained from limited computational resources. On the one hand, some *a priori* error estimates were first developed in parallel with the IGA framework in order to evaluate its convergence properties and compare to the classical FEA setting [7, 9]. On the other hand, and contrary to the wide literature available for FEA (see e.g. [81, 1, 59, 19] for an overview), few *a posteriori* error estimates are currently available for IGA in order to quantitatively estimate the distance between the unknown exact solution and its numerical approximation. However, they would represent useful tools to indicate on the error level and distribution, to identify areas where further refinement is needed, and thus to drive adaptive algorithms efficiently to achieve a given tolerance error. Most *a posteriori* error estimation tools which are currently available for IGA are essentially dedicated to linear elliptic problems. For instance, an *a posteriori* error estimate was introduced in [29], based on the hierarchical method initially developed in [6] for FEA, and in which the residual equation is approximately solved using hierarchical bases and bubble functions. Its reliability and efficiency is subjected to saturation assumption on the enlarged underlying space and the constants in the strengthened Cauchy inequality; consequently, bounding results are not guaranteed and problem dependent. In [85], a rather crude error assessment method was proposed for IGA; it consists of solving the residual equation with k-refinement steps, which may be very expensive. A goal-oriented error estimation procedure was developed in [53] for IGA computations, in which a classical dual-weighted residual (DWR) technique is used with p-refinement of the adjoint solution. In [52], a ZZ-type method with superconvergent patch recovery (SPR) was proposed to construct *a posteriori* error estimates in adaptive IGA; even though the method was developed for general meshes by computing superconvergent points, it is restricted to specific (i.e. scalar self-adjoint elliptic) problems for which superconvergence properties occur. A functional-type *a posteriori* error estimate was proposed in [50] leading to guaranteed and sharp upper bounds on the exact error in the energy norm provided constants can be accurately estimated or bounded (which is not always possible in practice). The previous method, using $H(div, \Omega)$ spaces which are easily reachable when considering NURBS basis functions, is closely related to the approach proposed in the present paper even though there are fundamental differences (e.g. the verification of balance equations is not imposed in [50] for the construction of the estimate). *A posteriori* error estimation for adaptive IGA boundary element methods with weakly-singular integral equations was addressed in [34]. Eventually, an *a posteriori* error estimate together with hierarchical B-splines local adaptivity were constructed in [15, 16] for elliptic second-order PDEs, using a residual-type error estimation method.

In the present work, we develop a robust and fully computable (i.e. with no unknown constants) *a posteriori* error estimate for IGA computations. For that purpose, we propose to use the Constitutive Relation Error (CRE) concept which has been extensively employed for FEA over the last 40 years (see [59, 62] for an overview). It provides for a general framework that enables to obtain such robust, accurate, and fully computable error bounds. In particular, and compared to the approach proposed in [50], it can be applied with irregular meshes, geometries, or solutions, still providing with accurate local estimates for mesh adaptation and avoiding large overestimations. Furthermore, a suitable advantage of this concept is that it naturally extends to nonlinear evolution problems such as viscoplasticity, contact, or damage, using thermodynamical considerations and convexity properties [57, 58]. In addition, it can be used for goal-oriented error estimation when employed in conjunction with adjoint techniques [17, 60, 18]. The CRE concept is based on duality and requires to recover fully equilibrated fields as all error estimation techniques providing for guaranteed and computable bounds [28, 64, 37, 13, 65]; this is the main technical issue, and this constitutes the scientific core of the paper. Among the various techniques which enable to perform such a recovery, we focus here on the hybrid-flux (or EET) technique initially developed in [54] then extended and enhanced in several works thereafter [55, 71, 74, 2]. Some alternative techniques for the construction of equilibrated fields can also be found in [69, 38, 32]. The hybrid-flux technique, in the FEA context, performs at the element level and involves the construction of equilibrated tractions on element edges before solving local and cheap Neumann problems on each element. We propose here to revisit this technique in order to extend it to IGA; the difficulty lies in the modified notion of locality for IGA basis functions (i.e. B-Spline or NURBS functions), as they have a larger support over knot spans than FE basis functions (Lagrange polynomials) have over elements. We show in the paper that equilibrated tractions can be recovered along knot spans boundaries, from the solution of local small size linear systems, before constructing equilibrated fields at the knot span level. The proposed procedure thus enables one to apply CRE error estimates for linear and nonlinear structural mechanics problems solved with IGA. It provides for an *a posteriori* error control either in a global way (i.e. in energy norm) or in a goal-oriented way (i.e. with respect to outputs of interest). The hybrid-flux technique being general (as merely based on balance equations), and in order to keep notations simple and avoid unnecessary details, we develop it for IGA on a simple scalar elliptic problem. Nevertheless, numerical applications with problems involving more elaborated mathematical models are provided to assess the performance and potential of the approach (in terms of behavior of the computed CRE estimate) for a large scope of structural mechanics activities. Moreover, we deliberately choose here not to address adaptive strategies with local mesh refinement too much, as they refer to classical and now well-known adaptivity techniques provided error estimates are available. However, as the scope of the paper is on the definition of such an estimate, we briefly describe how the construction of a CRE estimate can be performed for locally refined meshes, and we provide associated numerical results.

The paper is organized as follows: in Section 2, we introduce useful notations related to the IGA framework, and we define the reference problem as well as its IGA approximation; Section 3 is dedicated to the CRE concept for the computation of bounds on the discretization error, for both measure in the energy norm or with respect to specific outputs of interest; the construction of equilibrated fields in the IGA context, which is a requirement of the CRE concept and the main point of the paper, is detailed in Section 4; numerical results on two- and three-dimensional physical domains, with linear or nonlinear models are reported in Section 5; eventually, conclusions and prospects are drawn in Section 6. The paper is complemented with two appendices giving basics on B-Spline/NURBS functions, and the definition of the CRE functional for nonlinear structural mechanics models.

2. The IGA framework

2.1. Model problem

We consider a linear elliptic problem defined over a body occupying the closure of an open bounded domain $\Omega \subset \mathbb{R}^d$ (d=1, 2 or 3 being the space dimension), with regular Lipschitz boundary $\partial\Omega$. We assume that homogeneous Dirichlet boundary conditions are prescribed on a non-zero measured part $\partial_u\Omega \subset \partial\Omega$, whereas Neumann boundary conditions with given normal flux $F_d \in L^2(\partial_q\Omega)$ are prescribed on the complementary part $\partial_q\Omega \subset \partial\Omega$, with $\partial_u\Omega \cap \partial_q\Omega = \emptyset$ and $\overline{\partial_u\Omega \cup \partial_q\Omega} = \partial\Omega$. A given source term $f_d \in L^2(\Omega)$ may also be active in Ω. We denote by $\mathbb{K} \in [L^\infty(\Omega)]^{d\times d}$ the diffusion tensor, assumed to be symmetric, continuous and uniformly elliptic, i.e.:

$$\exists\alpha > 0, \exists\beta > 0 \text{ such that } \alpha|\boldsymbol{\tau}|^2 \leq \boldsymbol{\tau}\cdot\mathbb{K}\boldsymbol{\tau} \leq \beta|\boldsymbol{\tau}|^2 \quad \forall\boldsymbol{\tau} \in \mathbb{R}^d \tag{1}$$

The reference mathematical problem consists in finding the solution u (with associated flux $\mathbf{q} = \mathbb{K}\nabla u$) to the following system of equations:

$$\begin{aligned} -\nabla\cdot(\mathbb{K}\nabla u) &= f_d \quad \text{in } \Omega \\ u &= 0 \quad \text{on } \partial_u\Omega \\ \mathbb{K}\nabla u\cdot\mathbf{n} &= F_d \quad \text{on } \partial_q\Omega \end{aligned} \tag{2}$$

$\mathbf{n}$ denoting the unit outgoing normal vector to Ω. Introducing the functional space $\mathcal{U} = H_0^1(\Omega) = \{v \in H^1(\Omega), v_{|\partial_u\Omega} = 0\}$, the weak formulation of the problem reads:

$$\text{Find } u \in \mathcal{U} \text{ such that } a(u,v) = l(v) \quad \forall v \in \mathcal{U} \tag{3}$$

where bilinear form $a(\cdot,\cdot)$ and linear form $l(\cdot)$ are defined as:

$$a(u,v) = \int_\Omega \mathbb{K}\nabla u\cdot\nabla v\mathrm{d}\mathbf{x} \quad ; \quad l(v) = \int_\Omega f_d v\mathrm{d}\mathbf{x} + \int_{\partial_q\Omega} F_d v\mathrm{d}S \tag{4}$$

From the previous assumptions, and referring to the Lax-Milgram theorem, the mathematical problem (3) has a unique solution u, which will be taken as the reference when dealing with discretization error in the remainder of the paper. In addition, we introduce the energy norm $\|u\|_\mathbb{K} = \sqrt{a(u,u)}$ which is equivalent to the H^1-norm in $\mathcal{U}$. The norm $\|\cdot\|_\mathbb{K}$, directly linked to the properties of the problem operator, will be used in order to define a global measure of the discretization error.

2.2. *Representation of the domain geometry*

We consider the usual context in which the geometry of the physical domain Ω is described from CAD tools, that involve B-Spline functions or more generally NURBS functions. Univariate 1D B-Spline functions are piecewise polynomial functions $N_{i,p} : [a, b] \to \mathbb{R}$ of order p defined over a parametric space $[a, b]$. A basis of n B-Spline functions can be defined from a knot vector $\boldsymbol{\Xi} = \{a = \xi_1, \xi_2, \ldots, \xi_{n+p+1} = b\}$, in which the knots ξ_j are sorted in the ascending order (with possible multiplicity $r_j \leq p + 1$ of the same knot) and divide the parametric space into knot spans. The knot vector is said to be open when first and last knots have the maximal multiplicity $p + 1$ (the basis then becomes interpolatory at the boundary knots); in the paper, only open knots are considered. B-Spline basis functions $N_{i,p}$ $(i = 1, \ldots, n)$ are defined recursively from the knot vector $\boldsymbol{\Xi}$ using the Cox-de Boor algorithm; they are non-negative and non-zero in the interval $[\xi_i, \xi_{i+p+1}]$ only. Furthermore, the set of B-Spline functions constitutes a partition of unity ($\sum_{i=1}^{n} N_{i,p}(\xi) = 1$).
We may also introduce the vector $\boldsymbol{\Lambda} = \{\zeta_1, \ldots, \zeta_m\} \subset \boldsymbol{\Xi}$ of knots without repetitions, and the vector $\{r_1, \ldots, r_m\}$ of corresponding multiplicities (with $\sum_{j=1}^{m} r_j = n + p + 1$). A B-Spline of order p has at most C^{p-1} continuity; besides, at a knot ζ_j with multiplicity r_j, the number of continuous derivatives decreases to $p - r_j$ (so that multiplicity $r_j = p$ leads to C^0 continuity). A set of order 2 B-Spline functions is represented in Fig. 1.

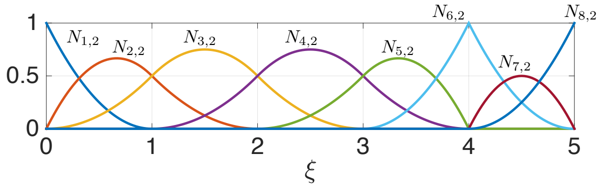

Figure 1: Quadratic basis functions for an open knot vector $\boldsymbol{\Xi} = \{0, 0, 0, 1, 2, 3, 4, 4, 5, 5, 5\}$.

Contrary to B-Spline functions, NURBS xfunctions have the ability to exactly describe conic geometries (such as circles of ellipses in 2D) which can not be exactly represented by polynomials. A set of n order p NURBS functions $R_{i,p} : [a, b] \to \mathbb{R}$ is constructed from the associated set of B-Spline functions $N_{i,p}$ by introducing additional weights w_j, $j = 1, \ldots, n$. The NURBS functions, which are then rational weighted spline functions, read:

$$R_{i,p}(\xi) = \frac{w_i N_{i,p}(\xi)}{\sum_{j=1}^{n} w_j N_{j,p}(\xi)} \tag{5}$$

NURBS functions inherit all properties of B-Spline functions (local support, partition of unity, pointwise non-negativity,...). When all weights are equal, the NURBS functions reduce to the B-Spline ones.

A set $\{N_{i,p}\}_{i=1}^{n}$ (resp. $\{R_{i,p}\}_{i=1}^{n}$) of B-Spline (resp. NURBS) functions of order p enables one to define parametric curves $\mathbf{C}^{BS} : [a,b] \rightarrow \mathbb{R}^d$ (resp. $\mathbf{C}^{NURBS} : [a,b] \rightarrow \mathbb{R}^d$), as:

$$\mathbf{C}^{BS}(\xi) = \sum_{i=1}^{n} \mathbf{B}_i N_{i,p}(\xi) \quad ; \quad \mathbf{C}^{NURBS}(\xi) = \sum_{i=1}^{n} \mathbf{B}_i R_{i,p}(\xi) \tag{6}$$

The n points $\mathbf{B}_i$ (coordinate vector of size $d \times 1$) are non-interpolatory control points that define the geometry of the curve. A piecewise linear interpolation between these control points defines the so-called control mesh (or polygon).

The extension to the definition of 2D (surface) or 3D (volume) geometrical entities can be easily performed using tensor product spaces with multi-variate functions. For instance, introducing the vector of space parameters $\boldsymbol{\xi} = \{\xi, \eta, \mu\}^T$ defined over a 3D domain or patch, parametric B-Spline and NURBS volumes can be described as:

$$\begin{aligned} \mathbf{V}^{BS}(\boldsymbol{\xi}) &= \sum_{i=1}^{n_1}\sum_{j=1}^{n_2}\sum_{k=1}^{n_3} \mathbf{B}_{i,j,k} \left(N_{i,p_1}(\xi) N_{j,p_2}(\eta) N_{k,p_3}(\mu)\right) = \sum_{A_{ijk}=1}^{n} \mathbf{B}_{A_{ijk}} N_{A_{ijk}}^{p_1,p_2,p_3}(\boldsymbol{\xi}) \\ \mathbf{V}^{NURBS}(\boldsymbol{\xi}) &= \sum_{i=1}^{n_1}\sum_{j=1}^{n_2}\sum_{k=1}^{n_3} \mathbf{B}_{i,j,k} \left(\frac{w_{i,j,k} N_{i,p_1}(\xi) N_{j,p_2}(\eta) N_{k,p_3}(\mu)}{\sum_{\hat{i}=1}^{n_1}\sum_{\hat{j}=1}^{n_2}\sum_{\hat{k}=1}^{n_3} w_{\hat{i},\hat{j},\hat{k}} N_{\hat{i},p_1}(\xi) N_{\hat{j},p_2}(\eta) N_{\hat{k},p_3}(\mu)} \right) \\ &= \sum_{A_{ijk}=1}^{n} \mathbf{B}_{A_{ijk}} R_{A_{ijk}}^{p_1,p_2,p_3}(\boldsymbol{\xi}) \end{aligned} \tag{7}$$

where $N_{i,p_1}(\xi)$, $N_{j,p_2}(\eta)$, and $N_{k,p_3}(\mu)$ are univariate B-Spline functions of order p_1, p_2, and p_3, respectively, $n = n_1.n_2.n_3$, and $A_{ijk} = n_1.n_2(k-1) + n_1(j-1) + i$.

Remark 1. The partition of unity property holding for univariate B-Splines or NURBS functions still holds in the context of multi-variate functions. Indeed, the following equality is straightforward:

$$\sum_{i=1}^{n_1}\sum_{j=1}^{n_2}\sum_{k=1}^{n_3} N_{i,p_1}(\xi) N_{j,p_2}(\eta) N_{k,p_3}(\mu) = \left(\sum_{i=1}^{n_1} N_{i,p_1}(\xi)\right)\left(\sum_{j=1}^{n_2} N_{j,p_2}(\eta)\right)\left(\sum_{k=1}^{n_3} N_{k,p_3}(\mu)\right) = 1 \tag{8}$$

From a domain $\Omega \subset \mathbb{R}^d$ with geometry described by B-Spline/NURBS functions, the construction by tensorization of d knot vectors Ξ^j ($j = 1, \ldots, d$) defined in each space dimension induces several description spaces that may be used (Fig. 2):

- the *index space*, formed by giving a unique integer value for each component, repeated or not, of the knot vectors. It identifies each knot (among $\Pi_{j=1}^{d}(n_j + p_j + 1)$ knots) and discriminates among knots having multiplicity greater than one;
- the *parametric space* $\overline{\Omega}$ which considers only non-zero intervals between knots (i.e. non-zero measured knot spans). Defining the set $\boldsymbol{\Lambda}^j \subset \Xi^j$ of m_j knots without repetitions in each direction, a regular mesh $\otimes_{j=1}^{d} \boldsymbol{\Lambda}^j$ made of $\Pi_{j=1}^{d}(m_j - 1)$ elements can be defined. In this space, lines or surfaces between knots constitute a natural definition of element boundaries;

- the *physical (real) space* Ω which provides for the geometrical representation of the domain. In this space, the location of control points and the definition of associated weights are design variables. Furthermore, a geometrical mapping $\mathbf{F}$ transforms coordinates of the parametric space to the physical space Ω, and conversely.

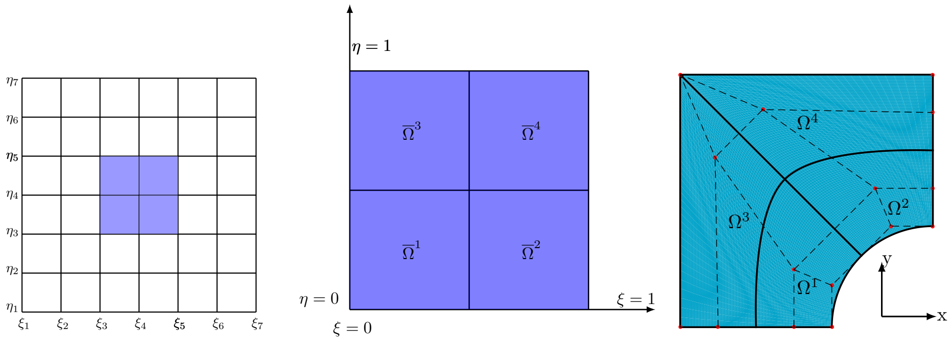

Figure 2: Index space (left), parametric space (center) and physical space with control mesh in dashed line (right) in a 2D representation with knot vectors $\mathbf{\Xi}^1 = \{0, 0, 0, 0.5, 1, 1, 1\}$ and $\mathbf{\Xi}^2 = \{0, 0, 0, 0.5, 1, 1, 1\}$.

Consequently, two meshes coexist in the physical space: (i) the *control mesh* which is defined by control points and does not conform to the geometry; (ii) the *physical mesh* which is a decomposition of the exact geometry (using possibly several patches) with non-zero measured knot spans; they are equivalent to elements in a FE mesh.

Further details on the use of B-Spline and NURBS functions to describe geometries can be found in [70, 45, 23].

2.3. IGA approximation and discretization error

In its original formulation, IGA consists of searching an approximate solution to (3) by means of a Galerkin formulation and a finite dimensional subspace of $\mathcal{U}$ spanned by the same set of B-Splines/NURBS basis functions as these describing the geometry of Ω. We thus introduce the functional space $\mathcal{U}_h = \text{Span}\{\varphi_I, 1 \leq I \leq n\} \cap \mathcal{U}$, where φ_I are defined from multi-variate B-Splines or NURBS functions introduced in Section 2.2 (e.g. $N^{p_1,p_2,p_3}_{A_{ijk}}$ or $R^{p_1,p_2,p_3}_{A_{ijk}}$ in 3D). The IGA formulation then reads:

$$\text{Find } u_h \in \mathcal{U}_h \text{ such that } a(u_h, v) = l(v) \quad \forall v \in \mathcal{U}_h \tag{9}$$

and leads to a linear system to solve. This formulation shares similarities with FEA as: (i) it is still based on an isoparametric formulation through the geometrical mapping $\mathbf{F}$; (ii) imposing boundary conditions is standard, provided open knot vectors are considered; (iii) the code architecture remains identical. However, and contrary to FEA, basis functions are now dictated by the geometrical model which is constructed during the design (CAD) process, prior to the analysis; therefore, IGA facilitates interaction with CAD. In this framework, the prescribed control points of the geometry play the role of (non-interpolating) nodes on

which dofs are defined.
Another major difference between FEA and IGA, which will be a main concern in Section 4, deals with locality properties of basis functions φ_I. Indeed, it is easy to show that order p B-Splines or NURBS functions are non-zero over $p+1$ knot spans (possibly with zero measure). Consequently, IGA basis functions are compactly supported but have an increased spatial support (for $p \geq 2$) compared to FEA. An illustration of this aspect is given in Fig. 3. A consequence is that the isoparametric mapping from the parameric space to the physical space is not local in the sense that it maps a cube (for $d = 3$) to many elements (defined as non-zero measured knot spans), not to a single element as in FEA. Considering for instance B-Spline functions N_I, the mapping for a given element (knot span) $\hat{\Omega}^e$ reads $\mathbf{F}_e(\boldsymbol{\xi}) = \sum_{I=1}^{n} N_I(\boldsymbol{\xi})\mathbf{x}_I^e$, and associated basis functions in the physical space read $\varphi_I = N_I \circ \mathbf{F}_e^{-1}$. Nevertheless, a standard Gauss quadrature is possible as in FEA, even though it has to be achieved in an additional parent space $[-1, 1]^d$. As a result, an extra (affine) mapping between the parametric space and the parent space is required. Then the information is transmitted to the physical space with the global mapping, and the assembly process is performed.

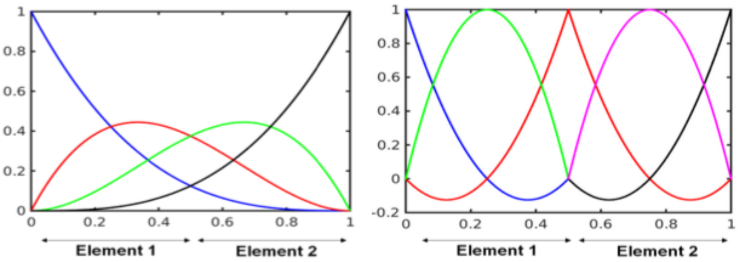

Figure 3: Quadratic 1D B-Spline and Lagrange functions for a mesh composed of two elements. The plots are realized in the parametric space $[0, 1]$.

In the following, we deal with the discretization error e_h associated with the formulation (9). It is defined as:

$$e_h = u - u_h \tag{10}$$

and may be measured either with a global measure $\mathcal{E}_{glob}$ defined from the energy norm ($\mathcal{E}_{glob} = \|e_h\|_{\mathbb{K}}$) or with a local measure $\mathcal{E}_Q$ defined with respect to an output of interest Q ($\mathcal{E}_Q = Q(e_h)$).

2.4. Mesh enrichment

Even though it is not the core of the paper, we briefly mention here some aspects related to mesh refinement in IGA, as it would be a natural adaptive process after computing error estimates, using marking at the knot span level or over larger subdomains. Furthermore, such enrichment techniques will be used for the computation of the error estimates proposed here (see Sections 3 and 4). There are actually flexible and very effective algorithms performing mesh refinement while exactly preserving the original geometry described at the coarsest level of discretization (Fig. 4). The adaptive procedure only refers to the initial representation of the geometry and does not require any feedback from CAD. The adaptive process enables

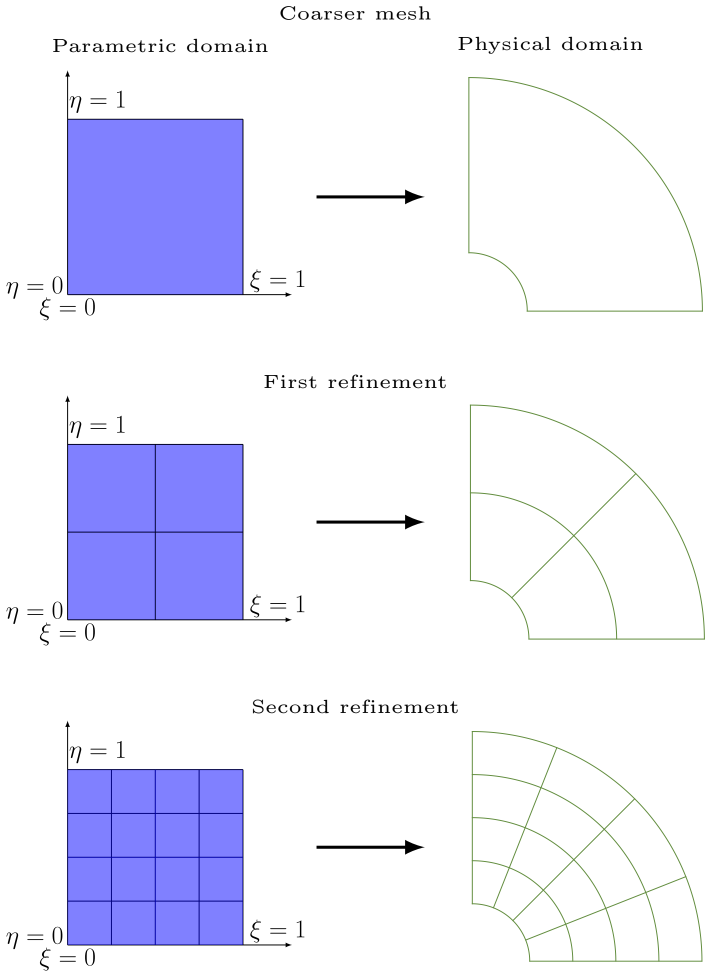

Figure 4: Mesh refinement with quadratic NURBS from open knot vectors $\boldsymbol{\Xi}^1 = \{0,0,0,1,1,1\}$ and $\boldsymbol{\Xi}^2 = \{0,0,0,1,1,1\}$. The geometrical map $\mathbf{F}$ and weighting functions w are unchanged during the refinement.

to control element size, order of the basis, but also continuity of the basis. There are three refinement techniques:

- h-refinement (see Fig. 5) which consists in knot insertion. Inserting new knots is associated with the automatic definition of new control points in order to preserve the initial geometry.
- p-refinement which consists in order elevation. It is achieved by order elevation and knot insertions at all knot positions in order to increase multiplicities r_j and preserve the continuity of the original curve.
- k-refinement (see Fig. 6), with higher order and higher continuity, which consists in order elevation and insertion of new knot values to define new elements across whose boundary functions will be C^{p-1}.

Due to the tensorized structure in the parametric space (see Section 2.2), IGA basis

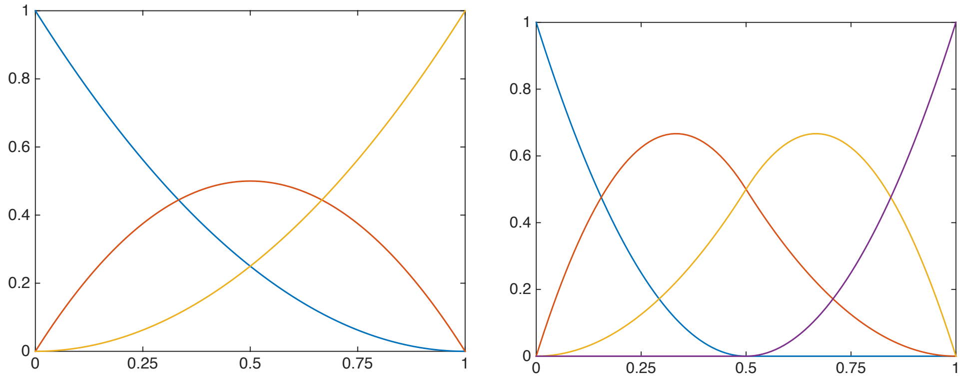

Figure 5: Illustration of h-refinement for $p = 2$, with knot insertion from $\Xi = \{0, 0, 0, 1, 1, 1\}$ (left) to $\Xi = \{0, 0, 0, 0.5, 1, 1, 1\}$ (right).

functions are not suited to local refinement (generating non-tensor product meshes) in their straightforward definition. However, advanced numerical tools have been investigated to address this issue, such as hierarchical B-Splines/NURBS with addition of local patches [36, 82, 75], locally-refinable splines (LR-splines) [47], truncated hierarchical B-Splines (THB-Splines) [40], polynomial splines over hierarchical T-meshes (PHT-splines) [26], localized multigrid resolution [20], or promising T-splines [78, 29] with T-junction (similar to hanging nodes in standard FEA). The interested reader is referred to the associated bibliography for further details.

3. Error estimation through the CRE concept

In this section, we define the CRE concept which provides for suitable *a posteriori* verification tools in order to assess the error between the exact solution u and the approximate IGA solution u_h.

3.1. CRE functional and properties

The CRE concept, explained in full details in [59, 62], has similitudes with various methods in the literature such as equilibrated residual [1] or flux-free [69, 21] approaches. They all share the idea of constructing a fully equilibrated dual field, which is actually the only way to recover guaranteed and fully computable error estimates in the energy norm. For the considered problem, the CRE concept applies to a so-called admissible solution $(\hat{u}, \hat{\mathbf{q}}) \in \mathcal{U} \times \mathcal{S}$ satisfying boundary conditions and balance equations of the model problem (2). The functional space $\mathcal{S}$ is defined as:

$$\mathcal{S} = \{\boldsymbol{\tau} \in H(div, \Omega), \int_\Omega \boldsymbol{\tau} \cdot \nabla v \mathrm{d}\mathbf{x} = \int_\Omega f_d v \mathrm{d}\mathbf{x} + \int_{\partial_q \Omega} F_d v \mathrm{d}S \quad \forall v \in \mathcal{U}\} \tag{11}$$

with $H(div, \Omega) = \{\boldsymbol{\tau} \in [L^2(\Omega)]^d, \nabla \cdot \boldsymbol{\tau} \in L^2(\Omega)\}$. Only the constitutive relation associated to diffusion is relaxed for such an admissible couple $(\hat{u}, \hat{\mathbf{q}})$. The CRE measure E_{CRE} computed

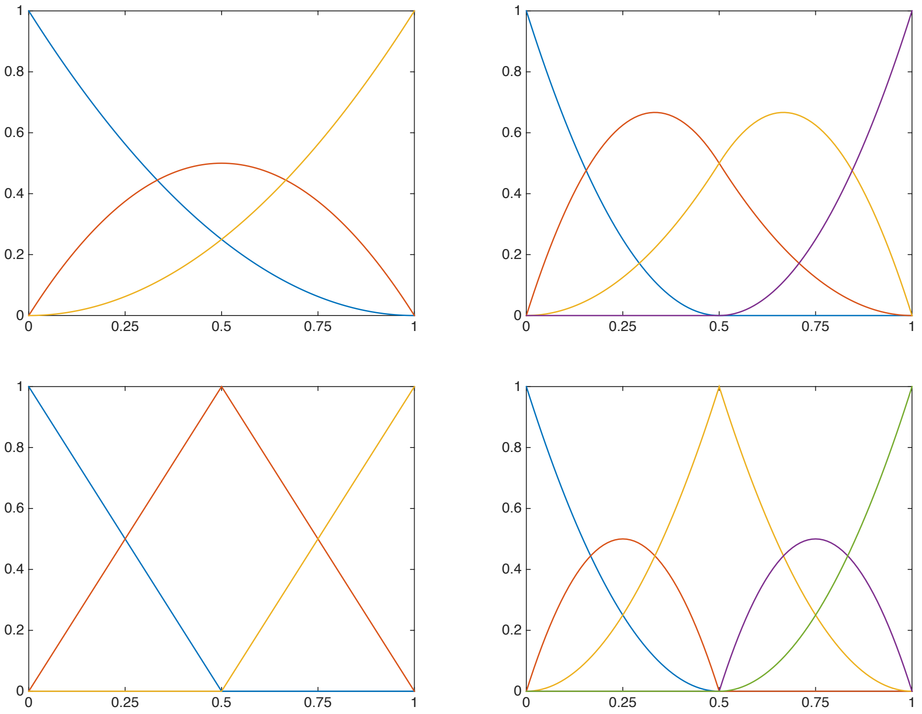

Figure 6: Illustration of k-refinement from an initial configuration with $p = 1$ and $\boldsymbol{\Xi} = \{0, 0, 1, 1\}$ (piecewise linear functions). Top: k-refinement using order elevation to $p = 2$ with $\boldsymbol{\Xi} = \{0, 0, 0, 1, 1, 1\}$ (left) then knot insertion with $\boldsymbol{\Xi} = \{0, 0, 0, 0.5, 1, 1, 1\}$ (right); it results in piecewise quadratic functions that are C^1 at internal knots. Bottom: alternative approach (similar to p-refinement) using knot insertion with $\boldsymbol{\Xi} = \{0, 0, 0.5, 1, 1\}$ (left) then order elevation to $p = 2$ with $\boldsymbol{\Xi} = \{0, 0, 0, 0.5, 0.5, 1, 1, 1\}$ (right); it results in piecewise quadratic functions that are C^0 at internal knots.

from $(\hat{u}, \hat{\mathbf{q}})$ is then a representative of the constitutive relation residual; it is defined as:

$$E^2_{CRE}(\hat{u}, \hat{\mathbf{q}}) = \int_\Omega (\hat{\mathbf{q}} - \mathbb{K}\nabla\hat{u}) \cdot \mathbb{K}^{-1}(\hat{\mathbf{q}} - \mathbb{K}\nabla\hat{u})\mathrm{d}\mathbf{x} = \|\hat{\mathbf{q}} - \mathbb{K}\nabla\hat{u}\|^2_{\mathbb{K}^{-1}} \tag{12}$$

where $\|\cdot\|_{\mathbb{K}^{-1}}$ is the energy norm in terms of flux over Ω. It is obvious that:

$$(u, \mathbf{q}) = \mathrm{argmin}_{(\hat{u},\hat{\mathbf{q}})\in\mathcal{U}\times\mathcal{S}} E^2_{CRE}(\hat{u}, \hat{\mathbf{q}}) \tag{13}$$

The Prager-Synge equality links the CRE measure E_{CRE} to a global measure (in the energy norm) of the discretization error between u and the considered admissible field $\hat{u} \in \mathcal{U}$:

$$E^2_{CRE}(\hat{u}, \hat{\mathbf{q}}) = \|\mathbf{q} - \hat{\mathbf{q}}\|^2_{\mathbb{K}^{-1}} + \|\mathbf{q} - \mathbb{K}\nabla\hat{u}\|^2_{\mathbb{K}^{-1}} \geq \|\mathbf{q} - \mathbb{K}\nabla\hat{u}\|^2_{\mathbb{K}^{-1}} = \|u - \hat{u}\|^2_{\mathbb{K}} \tag{14}$$

It results from the orthogonality property $\int_\Omega (\hat{\mathbf{q}} - \mathbf{q}) \cdot \mathbb{K}^{-1}(\mathbf{q} - \mathbb{K}\nabla\hat{u})\mathrm{d}\mathbf{x}$, with $\mathbf{q} = \mathbb{K}\nabla u$, which is ensured for any admissible couple $(\hat{u}, \hat{\mathbf{q}})$.

Choosing $\hat{u} = u_h \in \mathcal{U}$, and provided a flux field $\hat{\mathbf{q}} \in \mathcal{S}$ is available, the CRE measure thus defines a guaranteed and fully computable bound on the global error $\mathcal{E}_{glob}$.

Similarly, introducing the flux $\hat{\mathbf{q}}^* = \dfrac{1}{2}[\hat{\mathbf{q}} + \mathbb{K}\nabla\hat{u}]$ enables to derive a variant of the Prager-Synge equality:

$$E^2_{CRE}(\hat{u}, \hat{\mathbf{q}}) = 4\|\mathbf{q} - \hat{\mathbf{q}}^*\|^2_{\mathbb{K}^{-1}} \tag{15}$$

which is in practice used for goal-oriented error estimation (see Section 3.2).
Local error contributions can also be identified by means of the estimate E_{CRE} defined in (12). This merely comes down to defining local error indicators by splitting the estimate (in the integral form) over subregions (e.g. elements in FEA or knot spans in IGA). These contributions are in practice further used to implement effective adaptive procedures.

The construction of a relevant admissible flux field $\hat{\mathbf{q}} \in \mathcal{S}$, which determines the performance of the error estimate $E_{CRE}(\hat{u}, \hat{\mathbf{q}})$, is a key technical aspect of the procedure. It is the topic of Section 4, where we will show that an admissible flux field $\hat{\mathbf{q}}_h$ can be recovered from the IGA field $\mathbf{q}_h$ at hand.

Remark 2. An alternative to (14), when merely considering a flux field $\mathbf{z} \in H(\Omega, div) \supset \mathcal{S}$ (and $\partial_u\Omega = \partial\Omega$), reads:

$$\|\mathbf{q} - \mathbb{K}\nabla\hat{u}\|_{\mathbb{K}^{-1}} \leq \|\mathbf{z} - \mathbb{K}\nabla\hat{u}\|_{\mathbb{K}^{-1}} + C_\Omega\|\nabla \cdot \mathbf{z} + f_d\| \tag{16}$$

where C_Ω is the constant in the Friedrich's type inequality, which depends on matrix $\mathbb{K}$ and domain Ω, but not on the mesh. This inequality is used in [50] for *a posteriori* error estimation in IGA simulations. The recovery of $\mathbf{z} \in H(\Omega, div)$ (i.e. not fully equilibrated with the external loading contrary to $\hat{\mathbf{q}} \in \mathcal{S}$) is quite simple due to the regularity of IGA basis functions, but the practical use of (16) requires the evaluation of a constant which may be crude and lead to large over-estimations in the general case.

Remark 3. The CRE functional can be more generally defined as:

$$E^2_{CRE}(\hat{u}, \hat{\mathbf{q}}) = 2\int_\Omega [\psi(\nabla\hat{u}) + \psi^*(\hat{\mathbf{q}}) - \hat{\mathbf{q}} \cdot \nabla\hat{u}]\, \mathrm{d}\mathbf{x} \tag{17}$$

where ψ and ψ^* are dual (in the Legendre-Fenchel sense) convex potentials. For the considered model and constitutive law, these potentials are quadratic and read $\psi(\nabla v) = \frac{1}{2}\nabla v \cdot \mathbb{K}\nabla v$ and $\psi^*(\boldsymbol{\tau}) = \frac{1}{2}\boldsymbol{\tau} \cdot \mathbb{K}^{-1}\boldsymbol{\tau}$. This general formulation using potentials enables to define CRE estimates for complex nonlinear models such as viscoplasticity with or without softening [57, 58, 62], as illustrated in Section 5.4. A detailed presentation of the CRE functional in this context is given in AppendixA.

3.2. Goal-oriented error estimation

In many engineering applications, one is interested in specific quantities of interest. In such cases, energy-norm driven adaptive algorithms often fail to provide the required accuracy in these quantities. In order to construct strategies that minimize the number of dofs while providing the required accuracy of the solution in a given quantity of interest, the so-called goal-oriented adaptivity emerged. It is based on the definition of an adjoint problem [68, 73]. Following this classical adjoint-based technique, the CRE concept provides for error bounds on outputs as explained below.

We consider an output of interest, in terms of a linear functional $Q(u)$, and defined globally as:

$$Q(u) = \int_\Omega (\mathbf{q}_\Sigma \cdot \nabla u + f_\Sigma u) \mathrm{d}\mathbf{x} + \int_{\partial_q \Omega} F_\Sigma u \mathrm{d}S + \int_{\partial_u \Omega} \mathbf{Q}_\Sigma \cdot \nabla u \mathrm{d}S \tag{18}$$

Functions $\mathbf{q}_\Sigma$ and f_Σ, referred to as extraction operators or extractors, may be defined explicitly or implicitly (depending on the quantity Q). An adjoint problem is then defined from Q and from the adjoint operator of the problem. For the considered model, the operator is self-adjoint ($a = a^*$) so that the adjoint problem consists in finding $\tilde{u}$ (and $\tilde{\mathbf{q}} = \mathbb{K}\nabla\tilde{u}$) such that:

$$a(v, \tilde{u}) = a(\tilde{u}, v) = Q(v) \quad \forall v \in \mathcal{U} \tag{19}$$

Computing an approximate adjoint solution ($\tilde{u}_h, \tilde{\mathbf{q}}_h = \mathbb{K}\nabla\tilde{u}_h$) using IGA (with possibly different discretization parameters compared to the direct problem), then recovering an admissible flux field $\hat{\tilde{\mathbf{q}}} \in \tilde{\mathcal{S}}$ such that:

$$\int_\Omega \hat{\tilde{\mathbf{q}}} \cdot \nabla v \mathrm{d}\mathbf{x} = \int_\Omega (\mathbf{q}_\Sigma \cdot \nabla v + f_\Sigma v) \mathrm{d}\mathbf{x} + \int_{\partial_q \Omega} F_\Sigma v \mathrm{d}S + \int_{\partial_u \Omega} \mathbf{Q}_\Sigma \cdot \nabla v \mathrm{d}S \quad \forall v \in \mathcal{U} \tag{20}$$

it is possible to recover bounds on the error $\mathcal{E}_Q = Q(u) - Q(u_h)$. Indeed, it is easy to show that:

$$\begin{aligned}
\mathcal{E}_Q = a(u - u_h, \tilde{u}) &= \int_\Omega \nabla(u - u_h) \cdot \tilde{\mathbf{q}} \mathrm{d}\mathbf{x} \quad (\tilde{u} \text{ is solution to (19)}) \\
&= \int_\Omega \nabla(u - u_h) \cdot \hat{\tilde{\mathbf{q}}} \mathrm{d}\mathbf{x} \quad (\hat{\tilde{\mathbf{q}}} \in \tilde{\mathcal{S}}) \\
&= \int_\Omega \nabla(u - u_h) \cdot (\hat{\tilde{\mathbf{q}}} - \mathbb{K}\nabla\tilde{u}_h) \mathrm{d}\mathbf{x} + \int_\Omega \nabla(u - u_h) \cdot \mathbb{K}\nabla\tilde{u}_h \mathrm{d}\mathbf{x} \\
&= \int_\Omega \nabla(u - u_h) \cdot (\hat{\tilde{\mathbf{q}}} - \tilde{\mathbf{q}}_h) \mathrm{d}\mathbf{x} + \int_\Omega (\hat{\mathbf{q}} - \mathbf{q}_h) \cdot \nabla\tilde{u}_h \mathrm{d}\mathbf{x} \quad (\hat{\mathbf{q}} \in \mathcal{S}) \\
&= \int_\Omega (\mathbf{q} - \mathbf{q}_h) \cdot \mathbb{K}^{-1}(\hat{\tilde{\mathbf{q}}} - \tilde{\mathbf{q}}_h) \mathrm{d}\mathbf{x} + Q_{corr,1}
\end{aligned} \tag{21}$$

where $Q_{corr,1} = \int_\Omega (\hat{\mathbf{q}} - \mathbf{q}_h) \cdot \nabla\tilde{u}_h \mathrm{d}\mathbf{x}$ is a correction term on $Q(u_h)$, fully computable once $\hat{\mathbf{q}}$ is appropriately recovered. Using the Cauchy-Schwarz inequality together with (14) and (21) yields the guaranteed bound:

$$|\mathcal{E}_Q - Q_{corr,1}| \leq \|\mathbf{q} - \mathbf{q}_h\|_{\mathbb{K}^{-1}}.\|\hat{\tilde{\mathbf{q}}} - \tilde{\mathbf{q}}_h\|_{\mathbb{K}^{-1}} \leq E_{CRE}(u_h, \hat{\mathbf{q}}).E_{CRE}(\tilde{u}_h, \hat{\tilde{\mathbf{q}}}) \tag{22}$$

An improved bounding can be obtained introducing average fluxes $\hat{\mathbf{q}}^* = \frac{1}{2}[\hat{\mathbf{q}} + \mathbf{q}_h]$ and $\hat{\tilde{\mathbf{q}}}^* = \frac{1}{2}[\hat{\tilde{\mathbf{q}}} + \tilde{\mathbf{q}}_h]$. Indeed, rewriting (21) as:

$$\mathcal{E}_Q - Q_{corr,1} = \int_\Omega (\mathbf{q} - \hat{\mathbf{q}}^*) \cdot \mathbb{K}^{-1}(\hat{\tilde{\mathbf{q}}} - \tilde{\mathbf{q}}_h)\mathrm{d}\mathbf{x} + \int_\Omega (\hat{\mathbf{q}}^* - \mathbf{q}_h) \cdot \mathbb{K}^{-1}(\hat{\tilde{\mathbf{q}}}_h - \tilde{\mathbf{q}}_h)\mathrm{d}\mathbf{x} \tag{23}$$

and using the Cauchy-Schwarz inequality together with (15), the following improved bound holds:

$$|\mathcal{E}_Q - Q_{corr,2}| \leq \|\mathbf{q} - \hat{\mathbf{q}}^*\|_{\mathbb{K}^{-1}}.\|\hat{\tilde{\mathbf{q}}} - \tilde{\mathbf{q}}_h\|_{\mathbb{K}^{-1}} = \frac{1}{2}E_{CRE}(u_h, \hat{\mathbf{q}}).E_{CRE}(\tilde{u}_h, \hat{\tilde{\mathbf{q}}}) \tag{24}$$

with $Q_{corr,2} = Q_{corr,1} + \int_\Omega (\hat{\mathbf{q}}^* - \mathbf{q}_h) \cdot \mathbb{K}^{-1}(\hat{\tilde{\mathbf{q}}} - \tilde{\mathbf{q}}_h)\mathrm{d}\mathbf{x} = \int_\Omega (\hat{\mathbf{q}} - \mathbf{q}_h) \cdot \mathbb{K}^{-1}\hat{\tilde{\mathbf{q}}}^*\mathrm{d}\mathbf{x}$. This enables to define a computable bounding on the exact value $Q(u)$ of the quantity of interest, under the form:

$$Q^- \leq Q(u) \leq Q^+ \tag{25}$$

with

$$\begin{aligned} Q^- &= Q(u_h) + Q_{corr,2} - \frac{1}{2}E_{CRE}(u_h, \hat{\mathbf{q}}).E_{CRE}(\tilde{u}_h, \hat{\tilde{\mathbf{q}}}) \\ Q^+ &= Q(u_h) + Q_{corr,2} + \frac{1}{2}E_{CRE}(u_h, \hat{\mathbf{q}}).E_{CRE}(\tilde{u}_h, \hat{\tilde{\mathbf{q}}}) \end{aligned} \tag{26}$$

In practice, accurate bounds Q^- and Q^+ are obtained by an enrichment of the adjoint solution alone, so that $E_{CRE}(\tilde{u}_h, \hat{\tilde{\mathbf{q}}})$ tends to 0 and $Q_{corr,2}$ tends to $Q(u) - Q(u_h)$. Noticing that the adjoint loading $(\mathbf{q}_\Sigma, f_\Sigma, F_\Sigma, \mathbf{Q}_\Sigma)$ usually applies on a local subdomain of Ω, and therefore leads to an adjoint solution with localized high gradients (Saint-Venant principle), the idea is to use local enrichment in the vicinity of the space region of interest where the quantity Q is defined.

Remark 4. As an alternative to local mesh refinement, a non-intrusive approach (henceforth known as handbook technique) can be introduced for an accurate approximate solution of the adjoint problem [18, 61, 83]. It consists in introducing (handbook) enrichment functions for the construction of $\tilde{u}_h$, using a partition of unity property. Such an enrichment technique is particularly well-suited to handle pointwise quantities of interest, as enrichment functions then correspond to Green's functions, and this yields accurate error bounds without requiring to any regularization (e.g. mollification [73]) of the functional being considered or any specific local remeshing technique. We do not implement this technique in the present paper, even though it would particularly be of interest in the IGA context as no specific local mesh refinement technique would be required.

4. Construction of an admissible flux field

We detail in this section a procedure that enables to recover a relevant admissible flux field $\hat{\mathbf{q}}_h \in \mathcal{S}$ from a post-processing of the approximate IGA flux field $\mathbf{q}_h$ at hand, and using conventional tools available in commercial software. A similar procedure applies for the recovery of an admissible adjoint flux field $\hat{\tilde{\mathbf{q}}}_h \in \tilde{\mathcal{S}}$ from $\tilde{\mathbf{q}}_h$. This procedure essentially follows the same principles as the hybrid-flux (or EET) technique developed in the FEA context [54, 55, 71, 74]. Nevertheless, as IGA shape functions φ_I are associated with non-interpolating control points I (instead of physical nodes in FEA), and may be supported by a large number of knot spans (compared to FEA where the support of the shape function φ_I associated to node I is made of elements connected to this node alone), the EET technique requires specific modifications.

4.1. General hybrid-flux technique

The proposed procedure for the recovery of $\hat{\mathbf{q}}_h \in \mathcal{S}$ in the IGA context uses weak equilibration properties (9) of the IGA approximate flux field $\mathbf{q}_h = \mathbb{K}\nabla u_h \notin \mathcal{S}$ at hand. It involves local independent computations on (non-zero) knot spans Ω^e in the physical space, associated with tensorized regular (line, rectangle, parallelepiped) knot spans $\hat{\Omega}^e$ in the parametric space (see Section 2.2). Indeed, after defining an equilibrated traction field $\hat{F}^e$ on the boundary $\partial\Omega^e$ of each knot span Ω^e, the following Neumann problems are solved at the knot span level:

$$-\nabla \cdot \hat{\mathbf{q}}_h = f_d \quad \text{in } \Omega^e \quad ; \quad \hat{\mathbf{q}}_h \cdot \mathbf{n}^e = \hat{F}^e \quad \text{on } \partial\Omega^e \tag{27}$$

$\mathbf{n}^e$ being the unit outgoing normal vector to Ω^e. The recovery procedure is thus split in two steps which are detailed below.

4.1.1. Step 1: computation of equilibrated tractions on the boundary of knot spans

For each knot span Ω^e, equilibrated tractions $\hat{F}^e_\Gamma$ are computed on each edge/face Γ of $\partial\Omega^e$. These tractions should be such that:

$$\begin{aligned}
&\hat{F}^e_\Gamma = F_d \quad \text{if } \Gamma \subset \partial_q\Omega \quad \textit{(satisfaction of Neumann boundary conditions)}\\
&\int_{\Omega^e} f_d \mathrm{d}\mathbf{x} + \sum_{\Gamma\subset\partial\Omega^e} \int_\Gamma \hat{F}^e_\Gamma \mathrm{d}S = 0 \quad \forall\Omega^e \quad \textit{(satisfaction of equilibrium at the knot span level)}\\
&\hat{F}^e_\Gamma = \eta^e_\Gamma \hat{F}_\Gamma \quad \text{with } \eta^e_\Gamma = \pm 1 \quad \textit{(continuity of the normal admissible flux between knot spans)}
\end{aligned} \tag{28}$$

where $\hat{F}_\Gamma$ is a traction field specific to the edge/face Γ.

A key point to compute tractions $\hat{F}^e_\Gamma$ is the so-called prolongation condition, which is a local energy relation between the IGA field $\mathbf{q}_h$ and the recovered equilibrated field $\hat{\mathbf{q}}_h$. Denoting again by $\{\varphi_I\}_{1\leq I\leq N}$ the set of IGA basis functions (B-Splines or NURBS), the prolongation condition reads:

$$\int_{\Omega^e} (\hat{\mathbf{q}}_h - \mathbf{q}_h) \cdot \nabla\varphi_I \mathrm{d}\mathbf{x} = 0 \quad \forall\varphi_I, \forall\Omega^e \tag{29}$$

Using local properties (27) as well as the divergence theorem, (29) comes down to:

$$\sum_{\Gamma\subset\partial\Omega^e} \int_\Gamma \hat{F}^e_\Gamma \varphi_I \mathrm{d}S = \int_{\Omega^e} (\mathbf{q}_h \cdot \nabla\varphi_I - f_d\varphi_I)\mathrm{d}\mathbf{x} = Q^e_I \tag{30}$$

where Q_I^e is a computable quantity. For a given function φ_I, imposing (30) for all knot spans supporting φ_I leads to a small-size system of equations $\mathcal{S}_I$ to solve. It is important to notice that:

- ensuring (30) naturally enables to verify (28) due to the partition of unity property $\sum_{I=1}^n \varphi_I = 1$ ensured in the physical space (see Section 2.2);
- the unknowns of each system $\mathcal{S}_I$ are quantities $\int_\Gamma \hat{F}_\Gamma \varphi_I \mathrm{d}S$ i.e. projections, over φ_I, of unsigned tractions $\hat{F}_\Gamma$ on edge/face Γ of the physical mesh;
- each system $\mathcal{S}_I$ is usually rank deficient, but there is always at least one solution due to the weak equilibration property verified by $\mathbf{q}_h$ and resulting from (9). For a basis function φ_I vanishing on $\partial_q\Omega$, this reads $\sum_e Q_I^e = \int_\Omega (\mathbf{q}_h \cdot \nabla\varphi_I - f_d\varphi_I)\mathrm{d}\mathbf{x} = 0$;
- a unique solution for each system $\mathcal{S}_I$ may be obtained, if necessary, by the minimization of a cost function that involves the least square distances between unknowns $\int_\Gamma \hat{F}_\Gamma \varphi_I \mathrm{d}S$ and available average quantities $\int_\Gamma \langle \mathbf{q}_h \rangle \cdot \mathbf{n}\varphi_I \mathrm{d}S$. As the quantity $\mathbf{q}_h \cdot \mathbf{n}$ might be discontinuous across the interface Γ (even though is it usually not the case due to the classical use of high-order IGA basis functions), $\langle \mathbf{q}_h \rangle$ denotes the average of this field defined from values on the two knot spans connected to Γ.

After computing projection quantities $\int_\Gamma \hat{F}_\Gamma \varphi_I \mathrm{d}S$, (unsigned) tractions $\hat{F}_\Gamma$ can be recovered as a linear combination of IGA shape functions:

$$\hat{F}_\Gamma(\mathbf{x}) = \sum_{J \in \mathcal{J}_\Gamma} \hat{f}_\Gamma^J \varphi_{J|\Gamma}(\mathbf{x}) \tag{31}$$

where $\mathcal{J}_\Gamma$ denotes the set of indices for non-zero shape functions on Γ. Nevertheless, as non-zero functions $\varphi_{J|\Gamma}$ are usually not independent functions (contrary to the FEA case), projections on independent functions should be recovered in order to define invertible elementary matrix systems giving coefficients $\hat{f}_\Gamma^J$.

Details on the definition and solution of each system $\mathcal{S}_I$, as well as on the computation of coefficients $\hat{f}_\Gamma^J$, are given in Section 4.2 for an illustrative 2D case.

4.1.2. Step 2: local recovery of an equilibrated flux field

From the equilibrated traction field $\hat{F}^e$ computed in Step 1, an associated admissible flux field $\hat{\mathbf{q}}_h$ verifying (27) is recovered over each knot span Ω^e. The local equilibrium property (27) may be recast in a weak form as:

$$\int_{\Omega^e} \hat{\mathbf{q}}_h \cdot \nabla v \mathrm{d}\mathbf{x} = \int_{\Omega^e} f_d v \mathrm{d}\mathbf{x} + \int_{\partial\Omega^e} \hat{F}^e v \mathrm{d}S \quad \forall v \in \mathcal{U}(\Omega^e) \tag{32}$$

with $\mathcal{U}(\Omega^e) = H^1(\Omega^e)$. A (non-unique) solution to (32) can be obtained analytically, using polynomial functions with sufficiently high degree, provided the source term f_d is polynomial as well [56]. In practice, an alternative approach with numerical solution and higher-order enrichment is preferred. Indeed, the optimal flux field satisfying (32) is the one that minimizes over Ω^e the local contribution $\|\hat{\mathbf{q}}_h - \mathbf{q}_h\|_{\mathbb{K}^{-1}|\Omega^e}$ of the error estimate $E^2_{CRE}(u_h, \hat{\mathbf{q}}_h)$ (or equivalently minimizes $\|\hat{\mathbf{q}}_h\|_{\mathbb{K}^{-1}|\Omega^e})$. Duality arguments show that the underlying constrained minimization problem is equivalent to taking $\hat{\mathbf{q}}_{h|\Omega^e} = \mathbb{K}\nabla\rho$, with $\rho \in \mathcal{U}(\Omega^e)$ satisfying the following Neumann problem:

$$\int_{\Omega^e} \mathbb{K}\nabla\rho \cdot \nabla v \mathrm{d}\mathbf{x} = \int_{\Omega^e} f_d v \mathrm{d}\mathbf{x} + \int_{\partial\Omega^e} \hat{F}^e v \mathrm{d}S \quad \forall v \in \mathcal{U}(\Omega^e) \tag{33}$$

A numerical approximation of the solution of (33) is in practice obtained from an IGA approximation using mesh enrichment over the knot span Ω^e. In the remainder of the paper, we choose to use a k-refinement approach (see Section 2.4) with extra order 3; the final order of local basis functions is therefore $p+3$.

Remark 5. The flux field obtained from a numerical approximation of ρ is not rigorously equilibrated in each knot span Ω^e, which means that the error estimate computed from this flux field is not mathematically guaranteed. Nevertheless, choosing a $p+3$ order enables to obtain in practice a negligible error due to non-equilibrium in the computation of the CRE error estimate [5]. We also recall that when (32) is solved exactly with a dual approach (searching a solution flux with polynomial form for instance), fully guaranteed bounds are recovered from the CRE concept.

Remark 6. The solution of problem (33) is defined up to an additive constant (translation). This constant is fixed by imposing ρ to zero at an arbitrary point by means of a Lagrange multiplier.

4.2. Technical implementation on a 2D example

In this section, we focus on technical details related to Step 1 of the previously introduced procedure, i.e. the computation of equilibrated tractions. For this purpose, and in order the methodology to be easily understandable, we work in the parametric space (made of regular knot spans) instead of the physical space; we recall that they are related each other by means of a global mapping $\mathbf{F}$ in the isoparametric framework. Furthermore, in order to keep notations simple, we consider a two-dimensional parametric space with order 2 B-Spline functions and knot vectors $\mathbf{\Xi}^1 = [0, 0, 0, 1/3, 2/3, 1, 1, 1]$ and $\mathbf{\Xi}^2 = [0, 0, 0, 1/3, 2/3, 1, 1, 1]$ (see Fig. 7). Consequently, the parametric space is made of 3 knot spans and 5 functions in each direction (9 knot spans and 25 shape functions in the tensorized space). Tensorization results in the fact that basis functions read:

$$\varphi_I(\xi,\eta) = N_{i,2}(\xi).N_{j,2}(\eta) = N_i(\xi).N_j(\eta) \quad \text{or equivalently} \quad \varphi_I = N_i^\xi.N_j^\eta \quad (1 \leq i,j \leq 5) \tag{34}$$

where we simplified the notation $N_i = N_{i,2}$ for better readability. These functions are associated with control points $\mathbf{B}_I$ in order to define the exact geometry in the physical

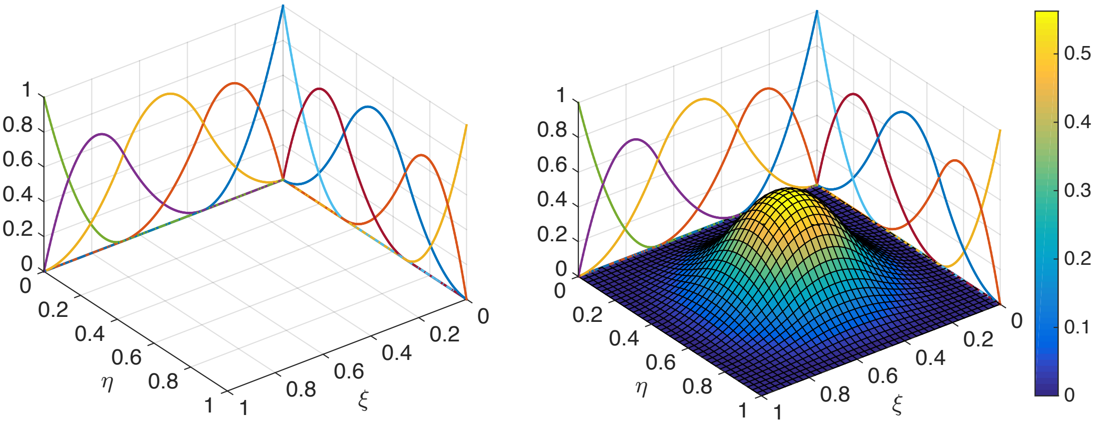

Figure 7: 2D parametric space and shape functions constructed from the tensorization of knot vectors $\boldsymbol{\Xi}^1$ and $\boldsymbol{\Xi}^2$ (left), and plot of the basis function $N_{3,2}(\xi)N_{3,2}(\eta)$.

space.
Similarly, each knot span in the parametric space reads:

$$\overline{\Omega}^e = \overline{\Omega}_1^{e_1} \times \overline{\Omega}_2^{e_2} \quad (1 \leq e_1, e_2 \leq 3) \tag{35}$$

where $\overline{\Omega}_d^{e_d}$ are 1D knot spans in the dimension d. In each 1D dimension, it can be easily seen that several functions may be non-zero at a given knot (interface between knot spans) compared to FEA where a single basis function is non-zero at each node position. Furthermore, the Cox-de Boor recursion formula leads to 3 (or $p+1$ in the general case) different basis functions supported by a given knot span, as illustrated in Fig. 8. The restrictions of these functions to each individual 1D knot span will be used as independent functions on which to perform projections and define expansions (31) of tractions $\hat{F}_\Gamma$.

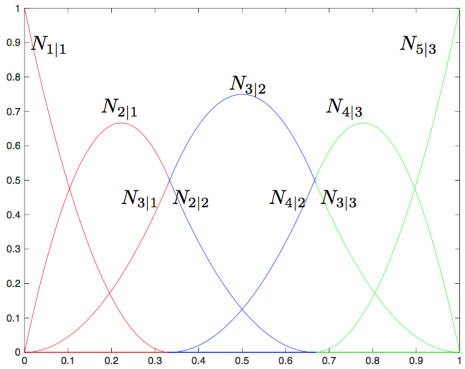

Figure 8: Restrictions of 1D B-Spline functions to knot span 1 (in red), 2 (in blue), and 3 (in green).

Coming back to the 2D parametric space, we then consider all shape functions which are non-zero at node positions (tensorization of knot positions). As an illustration, we consider the node i shown in Fig. 9, for which 4 functions are non-zero: $N_2^\xi.N_2^\eta$, $N_2^\xi.N_3^\eta$, $N_3^\xi.N_2^\eta$, and $N_3^\xi.N_3^\eta$. Consequently, 4 systems $\mathcal{S}_I$ associated to each of these basis functions φ_I and

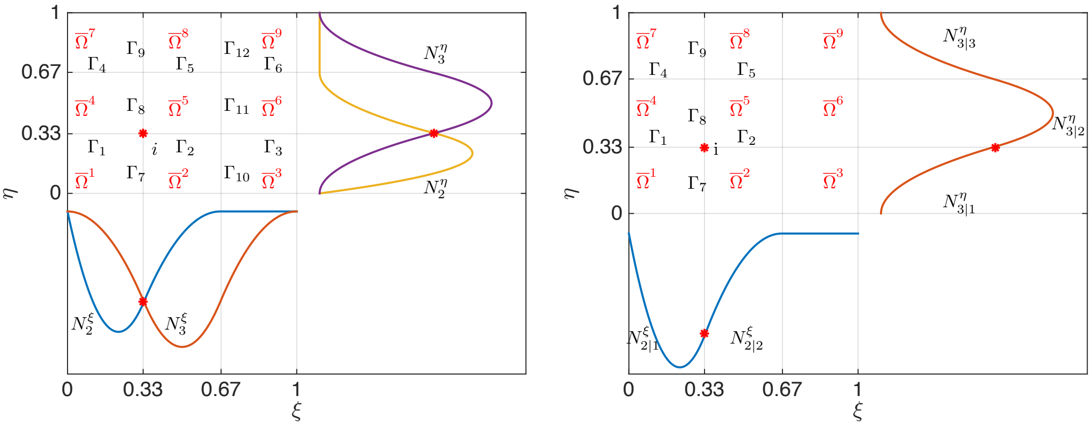

Figure 9: Definition of shape functions and edges associated with node i (left), and configuration at node i for the system associated to $\varphi_I = N_2^\xi.N_3^\eta$ (right).

resulting from (30) can be defined for this node (compared to one in classical FEA). They are defined over supports of each function as illustrated in Fig. 10.

In order to detail systems $\mathcal{S}_I$ for functions of the type $\varphi_I = N_i^\xi.N_j^\eta$, we introduce the following notations:

$$\int_{\Gamma_k} \hat{F}_{\Gamma_k} N_i^\xi.N_j^\eta \mathrm{d}S = \hat{b}_{\Gamma_k}^{ij} \quad ; \quad \int_{\overline{\Omega}^e} (\mathbf{q}_h \cdot \nabla(N_i^\xi.N_j^\eta) - f_d N_i^\xi.N_j^\eta)\mathrm{d}\boldsymbol{\xi} = Q_{ij}^e \tag{36}$$

4.2.1. Illustration of the system for $\varphi_I = N_2^\xi.N_3^\eta$

We use the numbering of Fig. 9, and write (30) for each knot span in the support of $N_2^\xi.N_3^\eta$. We thus come down to the configuration shown in Fig. 9, and the following system holds:

$$\begin{cases} \hat{b}_{\Gamma_1}^{23} - \hat{b}_{\Gamma_7}^{23} & = Q_{23}^1 \\ \hat{b}_{\Gamma_7}^{23} - \hat{b}_{\Gamma_2}^{23} & = Q_{23}^2 \\ \hat{b}_{\Gamma_8}^{23} - \hat{b}_{\Gamma_1}^{23} + \hat{b}_{\Gamma_4}^{23} & = Q_{23}^4 \\ \hat{b}_{\Gamma_2}^{23} - \hat{b}_{\Gamma_8}^{23} - \hat{b}_{\Gamma_5}^{23} & = Q_{23}^5 \\ \hat{b}_{\Gamma_9}^{23} - \hat{b}_{\Gamma_4}^{23} & = Q_{23}^7 \\ \hat{b}_{\Gamma_5}^{23} - \hat{b}_{\Gamma_9}^{23} & = Q_{23}^8 \end{cases} \tag{37}$$

where the sign convention used on the left-hand side follows the one which is arbitrarily employed for coefficients η_Γ^e and which is indicated on Fig. 10.

The previous system is simplified by gathering knot spans 4 and 7, and 5 and 8 (see Fig. 11), so that the system becomes small-sized and similar to the FEA context with

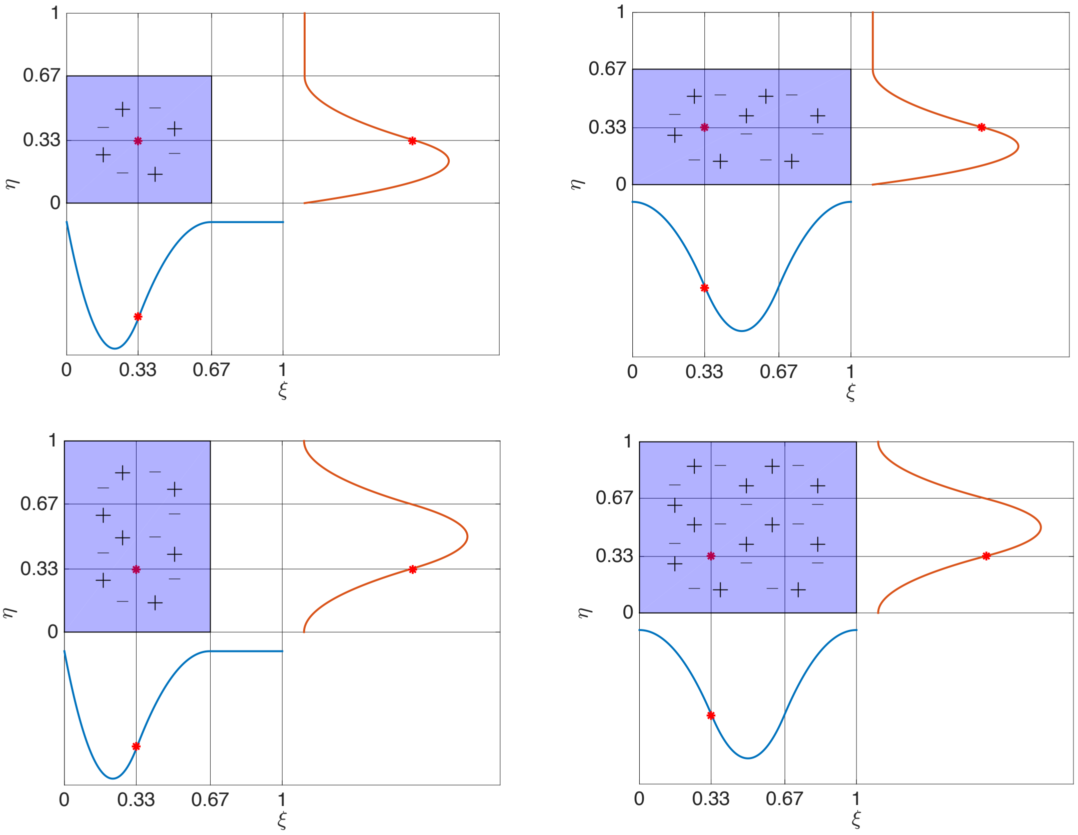

Figure 10: Support of the system $\mathcal{S}_I$ associated to basis function $N_2^\xi.N_2^\eta$ (top left), $N_3^\xi.N_2^\eta$ (top right), $N_2^\xi.N_3^\eta$ (bottom left), and $N_3^\xi.N_3^\eta$ (bottom right). The sign convention used for coefficients η_Γ^e is indicated.

interior node i. It reads:

$$\left\{\begin{array}{ll} \hat{b}_{\Gamma_1}^{23} - \hat{b}_{\Gamma_7}^{23} & = Q_{23}^1 \\ \hat{b}_{\Gamma_7}^{23} - \hat{b}_{\Gamma_2}^{23} & = Q_{23}^2 \\ \hat{b}_{\Gamma_8}^{23} + \hat{b}_{\Gamma_9}^{23} - \hat{b}_{\Gamma_1}^{23} & = Q_{23}^4 + Q_{23}^7 \\ \hat{b}_{\Gamma_2}^{23} - \hat{b}_{\Gamma_8}^{23} - \hat{b}_{\Gamma_9}^{23} & = Q_{23}^5 + Q_{23}^8 \end{array}\right. \tag{38}$$

Noticing that $Q_{23}^1 + Q_{23}^2 + Q_{23}^4 + Q_{23}^5 + Q_{23}^7 + Q_{23}^8 = 0$ (weak equilibration property (9) verified by $\mathbf{q}_h$), the previous system has an infinite number of solutions. The following cost function is then introduced:

$$\sum_{\Gamma \in \mathcal{G}} \left| \frac{\hat{b}_\Gamma^{23} - \bar{b}_\Gamma^{23}}{|\Gamma|} \right|^2 \tag{39}$$

with $\mathcal{G} = \{\Gamma_1, \Gamma_2, \Gamma_7, \Gamma_8, \Gamma_9\}$ and $\bar{b}_\Gamma^{23} = \int_\Gamma \langle \mathbf{q}_h \rangle \cdot \mathbf{n} N_2^\xi.N_3^\eta \mathrm{d}S$ ($\langle \mathbf{q}_h \rangle = \mathbf{q}_h$ here as C^1 functions are used). A constrained minimization is then performed to recover a unique solution to (38).

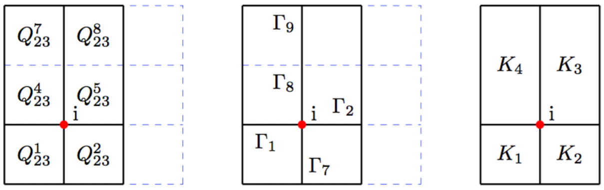

Figure 11: Illustration of the gathering of knot spans around node i.

4.2.2. Final projections and expansion of tractions

Using a similar procedure, systems $\mathcal{S}_I$ associated to node i and for basis functions $N_2^\xi.N_2^\eta$, $N_3^\xi.N_2^\eta$, and $N_3^\xi.N_3^\eta$ are solved (see Fig. 10). Values are thus obtained for the following unknowns:

- $\hat{b}_{\Gamma_1}^{22}$, $\hat{b}_{\Gamma_2}^{22}$, $\hat{b}_{\Gamma_7}^{22}$, $\hat{b}_{\Gamma_8}^{22}$ (for the system with basis function $N_2^\xi.N_2^\eta$);
- $\hat{b}_{\Gamma_1}^{23}$, $\hat{b}_{\Gamma_2}^{23}$, $\hat{b}_{\Gamma_7}^{23}$, $\hat{b}_{\Gamma_8}^{23}$, $\hat{b}_{\Gamma_9}^{23}$ (for the system with basis function $N_2^\xi.N_3^\eta$);
- $\hat{b}_{\Gamma_1}^{32}$, $\hat{b}_{\Gamma_2}^{32}$, $\hat{b}_{\Gamma_3}^{32}$, $\hat{b}_{\Gamma_7}^{32}$, $\hat{b}_{\Gamma_8}^{32}$ (for the system with basis function $N_3^\xi.N_2^\eta$);
- $\hat{b}_{\Gamma_1}^{33}$, $\hat{b}_{\Gamma_2}^{33}$, $\hat{b}_{\Gamma_3}^{33}$, $\hat{b}_{\Gamma_7}^{33}$, $\hat{b}_{\Gamma_8}^{33}$, $\hat{b}_{\Gamma_9}^{33}$ (for the system with basis function $N_3^\xi.N_3^\eta$).

Then, projections on edges over independent restrictions of 1D B-Spline functions (see Fig. 8) can be obtained as a linear combination (using the partition of unity property) of the previous values:

$$\begin{aligned}
&\int_{\Gamma_1} \hat{F}_{\Gamma_1} N_{2|1} \mathrm{d}S = \hat{b}_{\Gamma_1}^{22} + \hat{b}_{\Gamma_1}^{23} \quad ; \quad \int_{\Gamma_1} \hat{F}_{\Gamma_1} N_{3|1} \mathrm{d}S = \hat{b}_{\Gamma_1}^{32} + \hat{b}_{\Gamma_1}^{33} \\
&\int_{\Gamma_2} \hat{F}_{\Gamma_2} N_{2|2} \mathrm{d}S = \hat{b}_{\Gamma_2}^{22} + \hat{b}_{\Gamma_2}^{23} \quad ; \quad \int_{\Gamma_2} \hat{F}_{\Gamma_1} N_{3|2} \mathrm{d}S = \hat{b}_{\Gamma_2}^{32} + \hat{b}_{\Gamma_2}^{33} \\
&\int_{\Gamma_3} \hat{F}_{\Gamma_3} N_{3|3} \mathrm{d}S = \hat{b}_{\Gamma_3}^{32} + \hat{b}_{\Gamma_2}^{33} \\
&\int_{\Gamma_7} \hat{F}_{\Gamma_7} N_{2|1} \mathrm{d}S = \hat{b}_{\Gamma_7}^{22} + \hat{b}_{\Gamma_7}^{32} \quad ; \quad \int_{\Gamma_7} \hat{F}_{\Gamma_7} N_{3|1} \mathrm{d}S = \hat{b}_{\Gamma_7}^{23} + \hat{b}_{\Gamma_7}^{33} \\
&\int_{\Gamma_8} \hat{F}_{\Gamma_8} N_{2|2} \mathrm{d}S = \hat{b}_{\Gamma_8}^{22} + \hat{b}_{\Gamma_8}^{32} \quad ; \quad \int_{\Gamma_8} \hat{F}_{\Gamma_8} N_{3|2} \mathrm{d}S = \hat{b}_{\Gamma_8}^{23} + \hat{b}_{\Gamma_8}^{33} \\
&\int_{\Gamma_9} \hat{F}_{\Gamma_9} N_{3|3} \mathrm{d}S = \hat{b}_{\Gamma_9}^{23} + \hat{b}_{\Gamma_9}^{33}
\end{aligned} \tag{40}$$

Performing a similar approach for all nodes and all basis functions enables one to obtain all necessary projections, before recovering tractions themselves. For instance, considering the node j shown in Fig. 12 enables to recover the last projection on edge Γ_8:

$$\int_{\Gamma_8} \hat{F}_{\Gamma_8} N_{4|2} \mathrm{d}S = \hat{b}_{\Gamma_8}^{24} + \hat{b}_{\Gamma_8}^{34} \tag{41}$$

Eventually, the traction $\hat{F}_{\Gamma_8}$ is recovered as:

$$\hat{F}_{\Gamma_8}(\boldsymbol{\xi}) = \hat{f}_{\Gamma_8}^2 N_{2|2}(\boldsymbol{\xi}) + \hat{f}_{\Gamma_8}^3 N_{3|2}(\boldsymbol{\xi}) + \hat{f}_{\Gamma_8}^4 N_{4|2}(\boldsymbol{\xi}) \tag{42}$$

where coefficients $\hat{f}^2_{\Gamma_8}$, $\hat{f}^3_{\Gamma_8}$, and $\hat{f}^4_{\Gamma_8}$ are solutions of a small linear system involving known projections $\int_{\Gamma_8} \hat{F}_{\Gamma_8} N_{2|2} \mathrm{d}S$, $\int_{\Gamma_8} \hat{F}_{\Gamma_8} N_{3|2} \mathrm{d}S$, and $\int_{\Gamma_8} \hat{F}_{\Gamma_8} N_{4|2} \mathrm{d}S$. This system with symmetric matrix reads:

$$\begin{bmatrix} \int_{\Gamma_8} N^2_{2|2} \mathrm{d}S & \int_{\Gamma_8} N_{2|2}.N_{3|2} \mathrm{d}S & \int_{\Gamma_8} N_{2|2}.N_{4|2} \mathrm{d}S \\ \int_{\Gamma_8} N_{2|2}.N_{3|2} \mathrm{d}S & \int_{\Gamma_8} N^2_{3|2} \mathrm{d}S & \int_{\Gamma_8} N_{3|2}.N_{4|2} \mathrm{d}S \\ \int_{\Gamma_8} N_{2|2}.N_{4|2} \mathrm{d}S & \int_{\Gamma_8} N_{3|2}.N_{4|2} \mathrm{d}S & \int_{\Gamma_8} N^2_{4|2} \mathrm{d}S \end{bmatrix} \begin{pmatrix} \hat{f}^2_{\Gamma_8} \\ \hat{f}^3_{\Gamma_8} \\ \hat{f}^4_{\Gamma_8} \end{pmatrix} = \begin{pmatrix} \int_{\Gamma_8} \hat{F}_{\Gamma_8} N_{2|2} \mathrm{d}S \\ \int_{\Gamma_8} \hat{F}_{\Gamma_8} N_{3|2} \mathrm{d}S \\ \int_{\Gamma_8} \hat{F}_{\Gamma_8} N_{4|2} \mathrm{d}S \end{pmatrix} \tag{43}$$

The overall procedure for the construction of equilibrated tractions thus involves the solution of small-size independent systems, as in FEA.

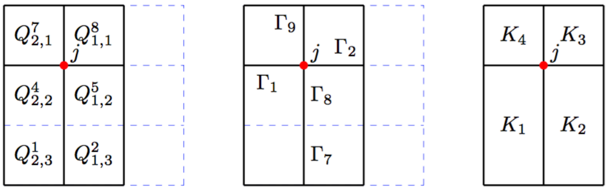

Figure 12: Illustration of the gathering of knot spans around node j, for the system with basis function $N^{\xi}_2.N^{\eta}_3$.

4.3. Generalization to locally refined meshes

The previous approach for the construction of an admissible field $\hat{\mathbf{q}}_h$, and in particular for the computation of equilibrated tractions $\hat{F}^e_{\Gamma}$, can also be used in the case of locally refined IGA meshes. Two cases should be considered:

- when hierarchical refinement is performed, with the local addition of patches representing finer details, the associated nested structure of the approximation space makes the extension of the hybrid-flux approach straightforward. The procedure for the construction of $\hat{F}^e_{\Gamma}$ naturally applies by using the prolongation condition over all shape functions as well as equilibrium properties in the IGA sense verified by the approximate solution. A numerical example dealing with hierarchical local refinement is given in Section 5.1;
- when T-splines are used, the local refinement procedure is equivalent to hanging nodes in the FEA context. Consequently, the extension of the hybrid-flux approach is not straightforward and should be conducted in a similar way as for FEA with hanging nodes (see [55] for instance). Nevertheless, this new procedure is out of the scope of the present paper.

5. Numerical results

In this section, we assess the performance of the error estimation approach based on CRE, considering 2D and 3D physical domains, and with linear or nonlinear mechanical models. In each case, the problem is chosen time-independent and the material is chosen isotropic. On average, the CPU time requested to compute global error estimates for all examples was 24% that associated to compute the approximate IGA solution. This results from the fact that many computations in the construction of the CRE estimate can be performed in parallel.

5.1. Example 1: thermal problem on a quarter of an annulus

We first consider a heat transfer problem (Poisson equation) on a quarter of annulus with prescribed homogeneous Dirichlet boundary conditions, similar to the one described in [50]. The physical domain Ω is defined as $(r,\theta) \in [R_i, R_e] \times [0, \pi/2]$ in a polar coordinates system, with $R_i = 1$ and $R_e = 4$. It is represented using order 2 NURBS basis functions in both directions of the parametric space (see Fig. 13), constructed from knot spans $\boldsymbol{\Xi}^1 = \{0,0,0,1,1,1\}$ and $\boldsymbol{\Xi}^2 = \{0,0,1,1\}$. The associated control points and weights are:

$$\begin{aligned}&\mathbf{B}_{1,1} = (0, R_i)\ ;\ w_{1,1} = 1\ ;\ \mathbf{B}_{2,1} = (R_i, R_i)\ ;\ w_{2,1} = 1/\sqrt{2}\ ;\ \mathbf{B}_{3,1} = (R_i, 0)\ ;\ w_{3,1} = 1\\ &\mathbf{B}_{1,2} = (0, R_e)\ ;\ w_{1,2} = 1\ ;\ \mathbf{B}_{2,2} = (R_e, R_e)\ ;\ w_{2,2} = 1/\sqrt{2}\ ;\ \mathbf{B}_{3,2} = (R_e, 0)\ ;\ w_{3,2} = 1\end{aligned} \tag{44}$$

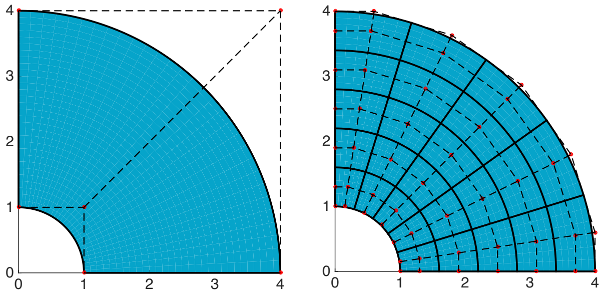

Figure 13: IGA representation of the geometry with control mesh (left), and initial discretization with 5 × 5 non-zero knot spans in the physical space. Control points are represented by red dots.

The problem reads:

$$-\Delta u = f \quad \text{in } \Omega \quad ; \quad u = 0 \quad \text{on } \partial\Omega \tag{45}$$

and the body force is chosen as:

$$\begin{aligned}f(x,y) = &(2x^4 + 2y^4 + 4x^2y^2 - 50x^2 - 50y^2 + 100)\sin(x)\sin(y)\\ &+ (68x - 8x^3 - 8xy^2)\cos(x)\sin(y)\\ &+ (68y - 8y^3 - 8x^2y)\sin(x)\cos(y)\end{aligned} \tag{46}$$

so that the exact solution $u(x,y)$ is analytical (manufactured solution): $u(x,y) = (x^2+y^2-1).(x^2+y^2-16).\sin(x).\sin(y)$. It is represented in Fig. 14.

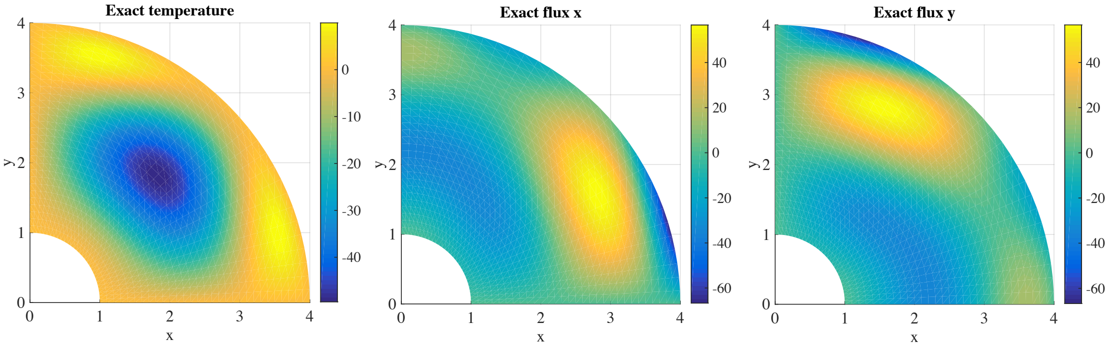

Figure 14: Exact solution for the 2D heat problem: u (left), $\mathbf{q} \cdot \mathbf{e}_x$ (center), and $\mathbf{q} \cdot \mathbf{e}_y$ (right).

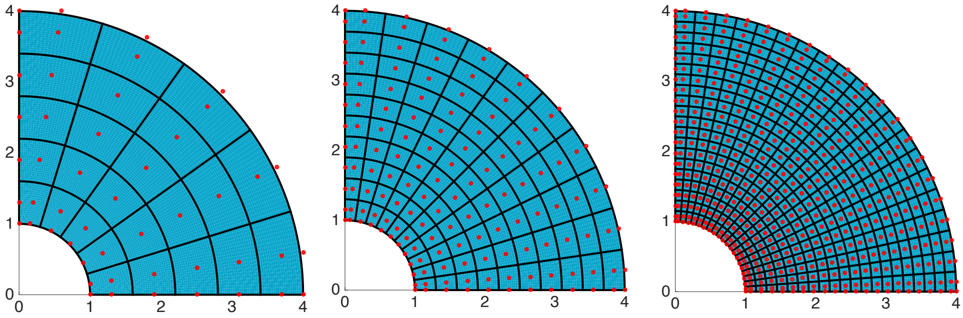

Figure 15: The various mesh sizes used, with 5×5 (left), 10×10 (center), and 20×20 (right) knot spans.

5.1.1. Estimation of the error in the energy norm

When approximating the exact solution by means of IGA, we investigate the accuracy and convergence of the CRE estimate $E_{CRE}(u_h, \hat{\mathbf{q}}_h)$ as an assessment of the exact discretization error in the energy norm $\mathcal{E}_{glob}$. For this purpose, we consider three uniform meshes with different mesh sizes as shown in Fig. 15. The approximate IGA flux field $\mathbf{q}_h$ obtained using the 5×5 mesh is represented in Fig. 16. For each mesh, we represent in Fig. 17, 18, and 19, respectively, the admissible flux field recovered from the approach of Section 4, as well as the associated CRE error map. For this problem, the value of the global effectivity index $i_{eff} = E_{CRE}/\|e_h\|_{\mathbb{K}}$ is lower than 1.11 for the 3 previous meshes considered. Furthermore, the maps of local effectivity indices (Fig. 20) show that the CRE estimate is a relevant and robust tool for mesh adaptation. Eventually, we plot in Fig. 21 the convergence of the CRE error estimate and effectivity index with respect to the number of dofs in uniform meshes. We particularly observe that the effectivity index tends to one when the number of dofs increases (i.e. the CRE estimate is asymptotically exact).

5.1.2. Performance with local mesh refinement

We now consider a locally refined mesh. It is constructed from an initial 10×10 mesh, after a first adaptation step from the error distribution shown in Fig. 18, and it involves hierarchical NURBS. It is obtained using hierarchical refinement tools available in the pack-

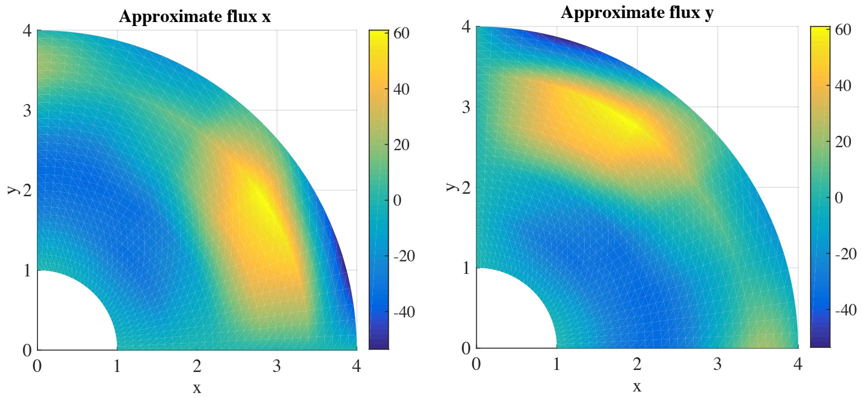

Figure 16: Approximate IGA flux field obtained with the 5×5 mesh: $\mathbf{q}_h \cdot \mathbf{e}_x$ (left) and $\mathbf{q}_h \cdot \mathbf{e}_y$ (right).

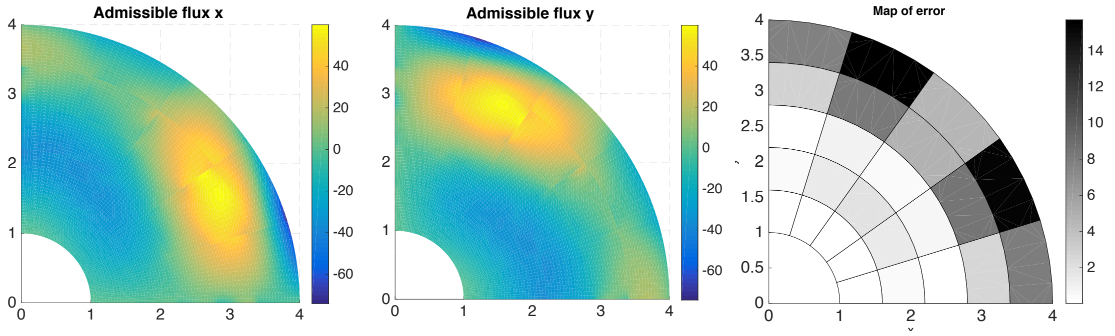

Figure 17: Admissible flux $\hat{\mathbf{q}}_h \cdot \mathbf{e}_x$ (left) and $\hat{\mathbf{q}}_h \cdot \mathbf{e}_y$ (center), and CRE error map (right) for the 5×5 mesh.

age available at *https://github.com/canitesc/IGAPack*. After applying the CRE approach to this mesh, we represent in Fig. 22 the spatial distribution of the error estimate and local effectivity indices. The global effectivity index is 1.054. Results indicate that the the CRE strategy still applies and performs well with a locally refined mesh.

5.1.3. Estimation of the error on quantities of interest

In this section, we investigate goal-oriented error estimation from the CRE framework. The first quantity of interest which is considered refers to a local average of the temperature field. It reads $Q_1 = \dfrac{1}{|\omega|}\displaystyle\int_\omega u(\mathbf{x})\mathrm{d}\mathbf{x}$ where ω is a local zone indicated in Fig. 23. This zone consists in a single knot span associated with the primal 5×5 mesh; as this mesh is fixed in this section, the local zone ω is fixed. In order to assess the discretization error on this quantity, we introduce the adjoint problem as described in Section 3.2. Its loading is made of a uniform body force $f_\Sigma = \dfrac{1}{|\omega|}$ applied in ω. The approximate solution obtained using IGA with a 10×10 mesh is given in Fig. 24. After computing an admissible adjoint flux field $\hat{\tilde{\mathbf{q}}}_h$, and the associated CRE error estimate $E_{CRE}(\tilde{u}_h, \hat{\tilde{\mathbf{q}}}_h)$, bounds on Q_1 can be obtained (see Section 3.2). We give in Fig. 25 the map of the admissible adjoint flux field

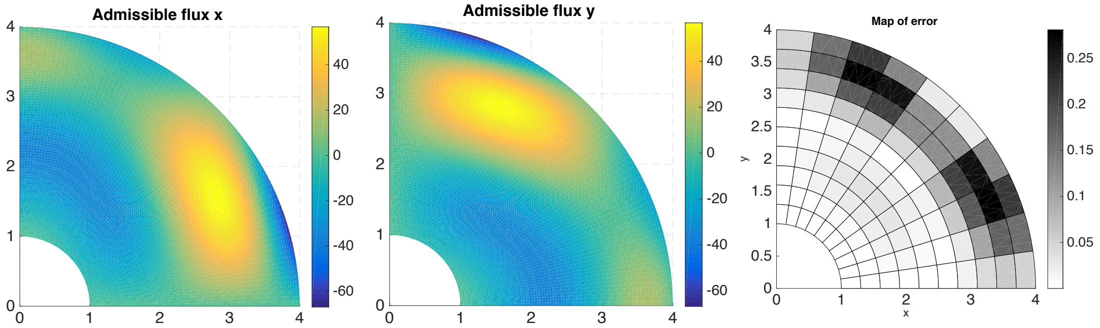

Figure 18: Admissible flux $\hat{\mathbf{q}}_h \cdot \mathbf{e}_x$ (left) and $\hat{\mathbf{q}}_h \cdot \mathbf{e}_y$ (center), and CRE error map (right) for the 10 × 10 mesh.

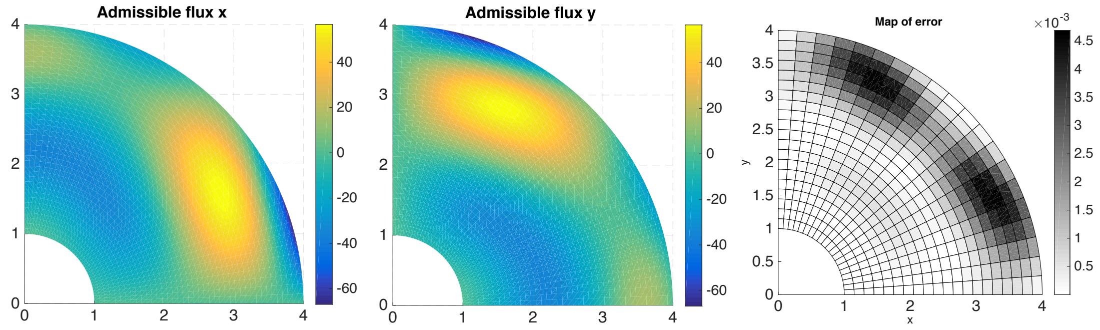

Figure 19: Admissible flux $\hat{\mathbf{q}}_h \cdot \mathbf{e}_x$ (left) and $\hat{\mathbf{q}}_h \cdot \mathbf{e}_y$ (center), and CRE error map (right) for the 20 × 20 mesh.

$\hat{\hat{\mathbf{q}}}_h$ and that of the CRE error estimate $E_{CRE}(\tilde{u}_h, \hat{\hat{\mathbf{q}}}_h)$. In addition, and from the bounding result (26), we represent in Fig. 23 the evolution of the relative bounds $Q_{1h}^-/(Q_{1h}^- + Q_{1h}^+)$ and $Q_{1h}^+/(Q_{1h}^- + Q_{1h}^+)$ with respect to the mesh size of the adjoint problem alone; here, the adjoint problem is refined uniformly. We observe that we get both accurate and guaranteed bounds on the quantity of interest Q_1, due to the fact that the CRE estimate for the adjoint problem decreases, and that the correction term $Q_{corr,2}$ (which involves both primal and adjoint approximate solutions) evolves, when refining the adjoint mesh.

As another quantity of interest, we now consider $Q_2 = \dfrac{1}{|\omega|} \displaystyle\int_\omega \mathbf{q}(\mathbf{x}) \cdot \mathbf{e}_x \mathrm{d}\mathbf{x}$. The loading of the associated adjoint problem consists of a uniform pre-flux field inside ω. After computing an approximate adjoint solution using IGA with a 10 × 10 mesh, then an admissible flux field, the CRE error estimate $E_{CRE}(\tilde{u}_h, \hat{\hat{\mathbf{q}}}_h)$ is obtained; its spatial distribution is represented in Fig. 26. We also represent in Fig. 26 the evolution of the relative bounds $Q_{2h}^-/(Q_{2h}^- + Q_{2h}^+)$ and $Q_{2h}^+/(Q_{2h}^- + Q_{2h}^+)$ with respect to the mesh size of the adjoint problem alone. We again observe that very accurate bounds on the quantity of interest Q_2 (or on the error $\mathcal{E}_{Q_2}$) is obtained.

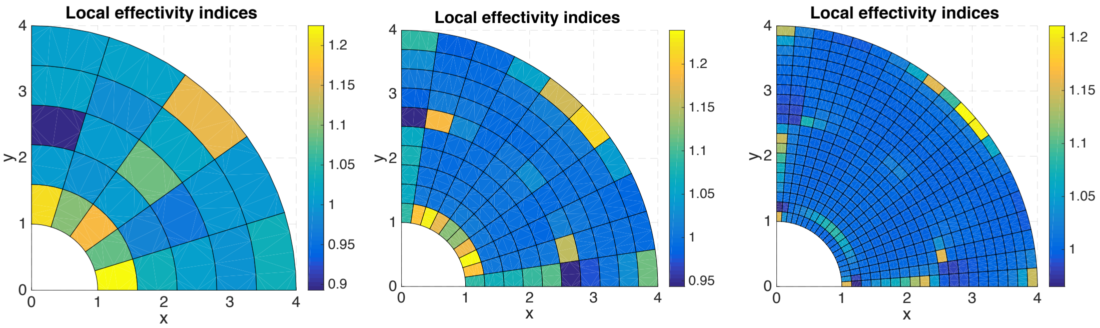

Figure 20: Maps of local effectivity indices for the three mesh sizes considered.

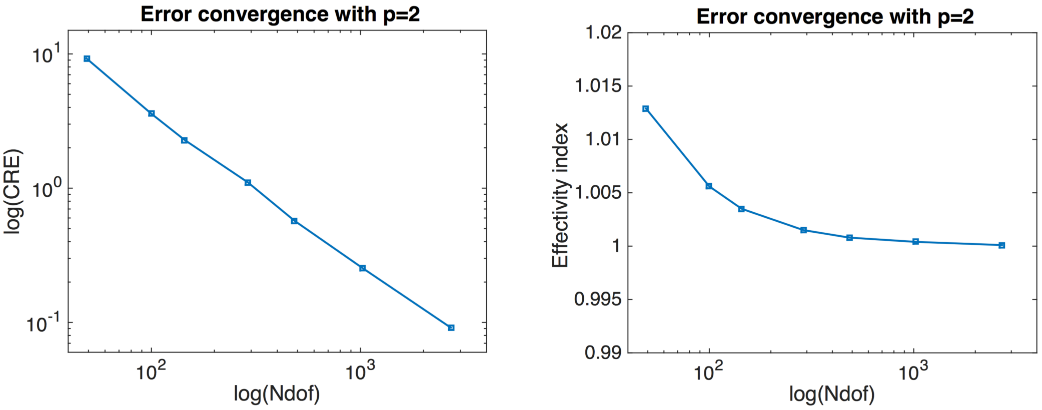

Figure 21: Convergence of the error estimate (left) and effectivity index (right) with respect to the number of dofs.

5.1.4. *Performance with higher order IGA*

We now investigate the performance of the estimate for higher IGA order, i.e. $p = 3$ and $p = 4$. Considering $p = 3$ first, we show in Fig. 27 (resp Fig. 28) the distribution of the CRE estimate (resp. of the local effectivity indices) for regular 5×5, 10×10, and 20×20 meshes. In Fig. 29, we represent the convergence of the CRE estimate and the global effectivity index with respect to the number of dofs in uniform meshes. Similar plots are given for $p = 4$ in Figs. 30, 31, and 32.

As for $p = 2$, we observe a correct behavior and asymptotic exactness of the estimate, with performance comparable with that exhibited in [50, 52]. This illustrates that the CRE estimate is robust for any order p.

5.2. *Example 2: elasticity problem on a L-shape domain*

We now investigate a non-smooth linear elasticity problem on a domain Ω consisting of a L-shape console beam (see Fig. 33), as described in [50, 82]. The domain is defined as $\Omega = [-1, 1]^2 \backslash [0, 1]^2$, and specific Dirichlet boundary conditions are prescribed as shown in Fig. 33. The material parameters are $E = 1$ (Young modulus) and $\nu = 0.3$ (Poisson ratio). Order 2 basis functions are used in both directions of the parametric space; they

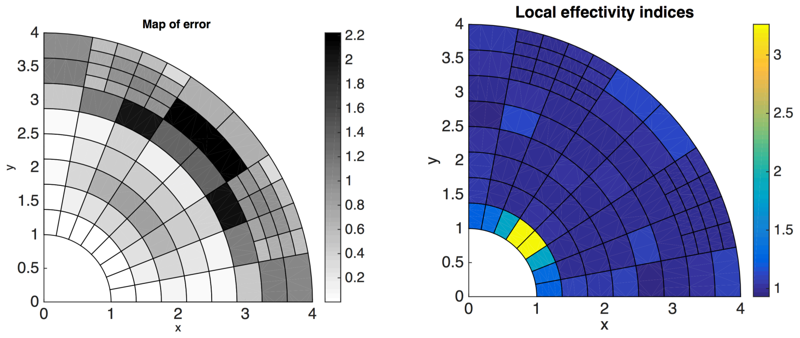

Figure 22: Map of the CRE error estimate (left) and of the local effectivity indices (right) for a locally refined mesh.

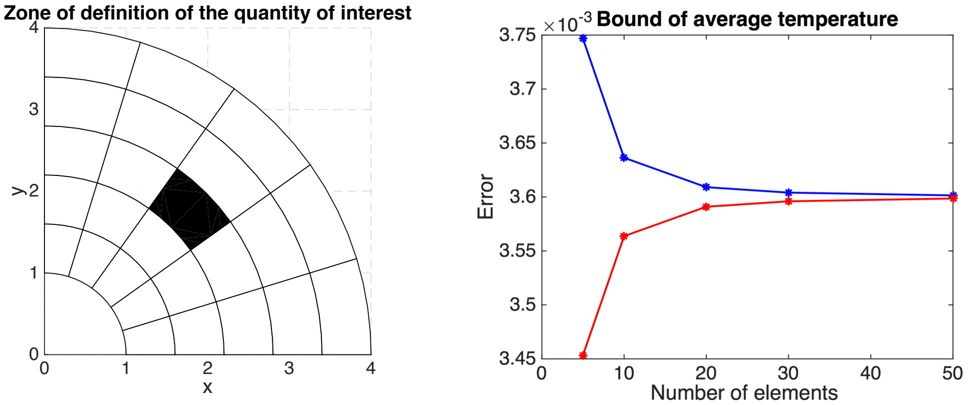

Figure 23: Definition of the local zone ω over which the quantity of interest Q_1 is defined (left), and evolution of the relative bounds $Q_{1h}^{-}/(Q_{1h}^{-}+Q_{1h}^{+})$ and $Q_{1h}^{+}/(Q_{1h}^{-}+Q_{1h}^{+})$ with respect to the adjoint mesh size (right).

are constructed from knot spans $\mathbf{\Xi}^1 = \{0,0,0,0.5,1,1,1\}$ and $\mathbf{\Xi}^2 = \{0,0,0,1,1,1\}$, and the associated control points (with weights $w_{i,j} = 1$) are:

$$\begin{aligned} &\mathbf{B}_{1,1} = (0,4)\ ;\ \mathbf{B}_{2,1} = \mathbf{B}_{3,1} = (0,0)\ ;\ \mathbf{B}_{4,1} = (4,0) \\ &\mathbf{B}_{1,2} = (1,4)\ ;\ \mathbf{B}_{2,2} = (1,2)\ ;\ \mathbf{B}_{3,2} = (2,1)\ ;\ \mathbf{B}_{4,2} = (4,1) \\ &\mathbf{B}_{1,3} = (2,4)\ ;\ \mathbf{B}_{2,3} = \mathbf{B}_{3,3} = (2,2)\ ;\ \mathbf{B}_{4,3} = (4,2) \end{aligned} \tag{47}$$

The approximate IGA solution in terms of displacement and stress fields is given in Figs. 34 and 35, respectively.

5.2.1. *Performance of the estimate on regular meshes*

The interest of this problem is to check that the estimate enables to accurately detect the local error due to the singularity at the re-entrant corner. After computing admissible fields, the map of the CRE estimate is given in Fig. 36 for several uniform meshes with 10 × 10, 20 × 20, or 30 × 30 knot spans. These maps clearly indicate that the major error source is located at the singularity. Furthermore, the global effectivity index is between 1.12 and 1.17 for all meshes.

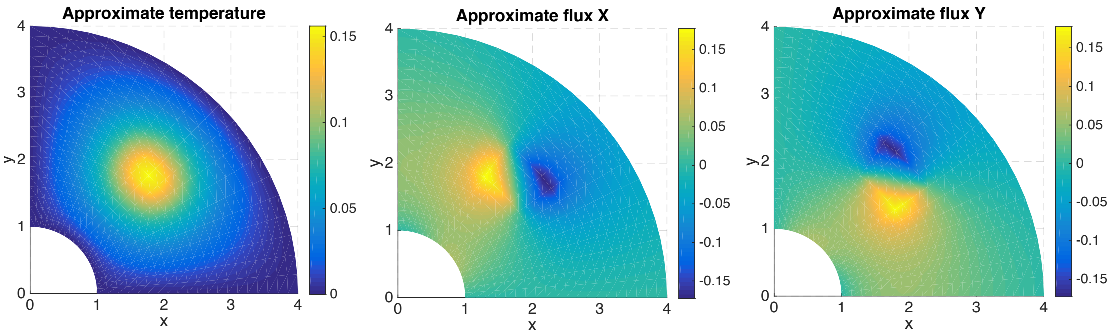

Figure 24: Approximate IGA adjoint solution: $\tilde{u}_h$ (left), $\tilde{\mathbf{q}}_h \cdot \mathbf{e}_x$ (center), and $\tilde{\mathbf{q}}_h \cdot \mathbf{e}_y$ (right).

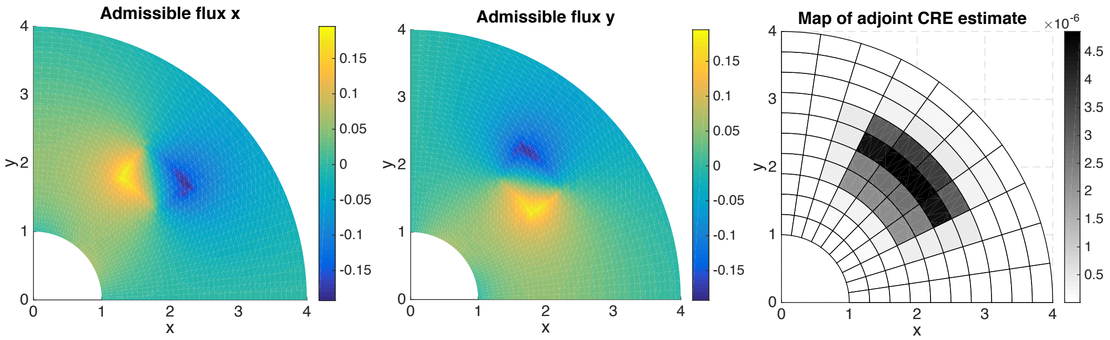

Figure 25: Adjoint flux field $\hat{\tilde{\mathbf{q}}}_h \cdot \mathbf{e}_x$ (left) and $\hat{\tilde{\mathbf{q}}}_h \cdot \mathbf{e}_y$ (center), and map of the adjoint CRE estimate (right).

5.2.2. *Performance of the estimate on highly graded meshes*

We investigate here the robustness of the estimate when considering highly graded meshes. For that, we generate meshes after modifying dimensions of the L-shape domain. While keeping a bulk square domain of size 2×2, we shorten the length of the two edges located in the vicinity of the re-intrant corner. This is changed from 2 (initial L-shape configuration of the previous section) to 0.2 (Case 1) or 0.1 (Case 2). The resulting maps of the CRE estimate and local effectivity indices are indicated in Fig. 37. They indicate as expected that local effectivity indices deteriorate in very distorted elements, as observed for FEA; better results could be obtained using the approach developed in [35, 72] and based on local energy minimizations when computing the admissible flux/stress fields. Nevertheless, the global error estimation with CRE remains relevant as the global effectivity index is 1.27 for Case 1 and 1.34 for Case 2.

5.3. *Example 3: thermal problem on a 3D structure*

We consider here the 3D geometry shown in Fig. 38. It is a quarter of hollow cylinder with height $h = 3$, external radius $R_e = 4$, and internal radius $R_i = 1$. The geometry is represented using NURBS basis functions constructed from knot spans $\boldsymbol{\Xi}^1 = \{0, 0, 0, 1, 1, 1\}$,

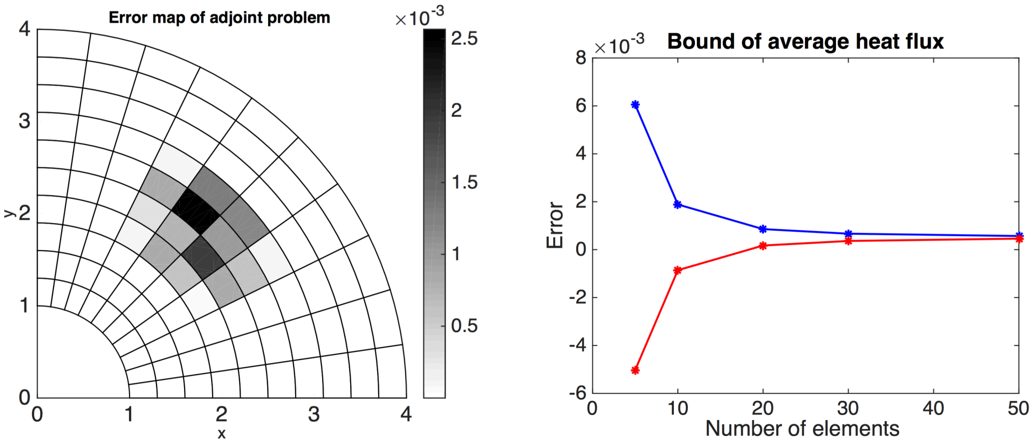

Figure 26: Map of the adjoint CRE estimate for the quantity of interest Q_2 (left), and evolution of the relative bounds $Q^-_{2h}/(Q^-_{2h}+Q^+_{2h})$ and $Q^+_{2h}/(Q^-_{2h}+Q^+_{2h})$ with respect to the adjoint mesh size (right).

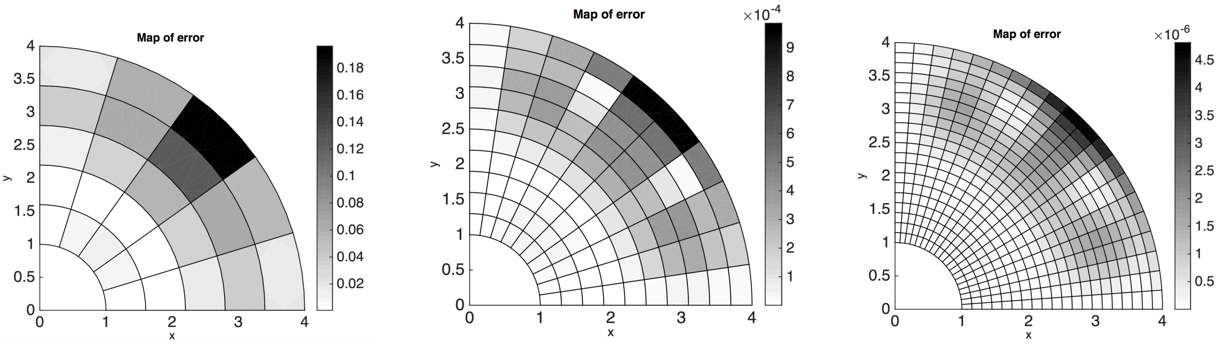

Figure 27: Map of the CRE estimate for the 5×5, 10×10, and 20×20 meshes (from left to right) and $p = 3$.

$\Xi^2 = \{0,0,1,1\}$, and $\Xi^3 = \{0,0,1,1\}$. The associated control points and weights are:

$$\begin{aligned}
&\mathbf{B}_{1,1} = (0, R_i, 0)\ ;\ w_{1,1} = 1\ ;\ \mathbf{B}_{2,1} = (R_i, R_i, 0)\ ;\ w_{2,1} = 1/\sqrt{2}\ ;\ \mathbf{B}_{3,1} = (R_i, 0, 0)\ ;\ w_{3,1} = 1\\
&\mathbf{B}_{1,2} = (0, R_e, 0)\ ;\ w_{1,2} = 1\ ;\ \mathbf{B}_{2,2} = (R_e, R_e, 0)\ ;\ w_{2,2} = 1/\sqrt{2}\ ;\ \mathbf{B}_{3,2} = (R_e, 0, 0)\ ;\ w_{3,2} = 1\\
&\mathbf{B}_{1,3} = (0, R_i, h)\ ;\ w_{1,3} = 1\ ;\ \mathbf{B}_{2,3} = (R_i, R_i, h)\ ;\ w_{2,3} = 1/\sqrt{2}\ ;\ \mathbf{B}_{3,3} = (R_i, 0, h)\ ;\ w_{3,3} = 1\\
&\mathbf{B}_{1,4} = (0, R_e, h)\ ;\ w_{1,4} = 1\ ;\ \mathbf{B}_{2,4} = (R_e, R_e, h)\ ;\ w_{2,4} = 1/\sqrt{2}\ ;\ \mathbf{B}_{3,4} = (R_e, 0, h)\ ;\ w_{3,4} = 1
\end{aligned} \tag{48}$$

A uniform body force $f_d = 1$ is applied in the domain Ω, while homogeneous Dirichlet boundary conditions are prescribed on the whole boundary $\partial\Omega$. The approximate solution is given in Fig. 39.

After computing admissible fields and the CRE estimate for this 3D structure, we observe that the global effectivity index is 1.17. The map of the CRE estimate is given in Fig. 40. Similar evolutions of the estimate to those shown for previous examples are observed when increasing the number of dofs or the IGA order.

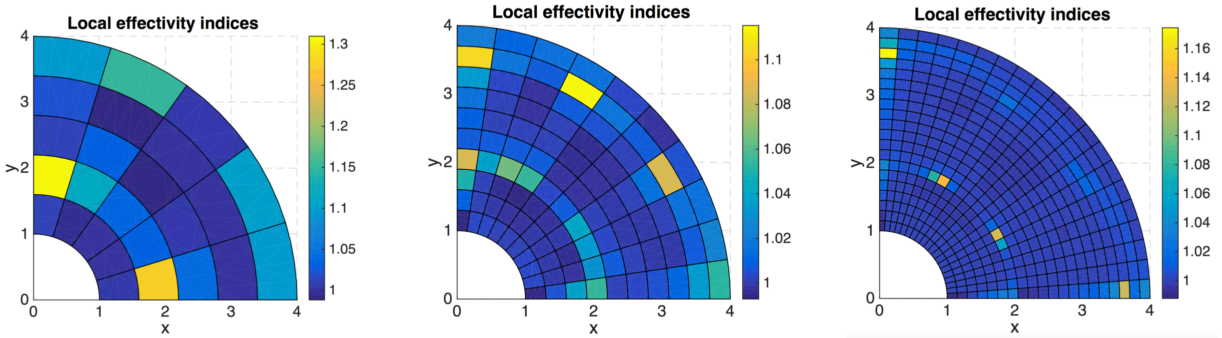

Figure 28: Map of local effectivity indices for the 5×5, 10×10, and 20×20 meshes (from left to right) and $p = 3$.

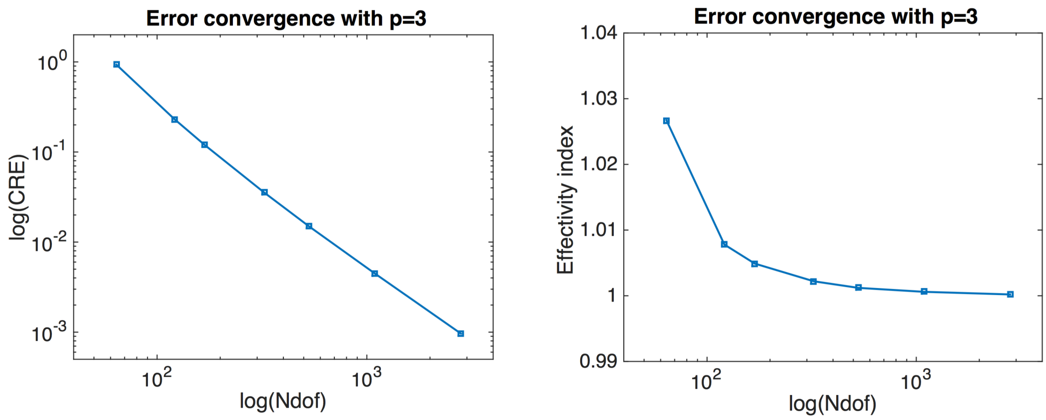

Figure 29: Convergence of the CRE estimate (left) and the global effectivity index (right) with respect to the number of dofs for $p = 3$.

5.4. Example 4: nonlinear problem on a plate with circular hole

As a final example, we consider a nonlinear damage problem (elasticity with isotropic softening) on a plate with circular hole under in-plane tension, as described in [82]. The geometry is represented using NURBS basis functions constructed from knot spans $\Xi^1 = \{0, 0, 0, 0.5, 1, 1, 1\}$ and $\Xi^2 = \{0, 0, 0, 1, 1, 1\}$. The associated control points and weights are:

$$\begin{gathered}
\mathbf{B}_{1,1} = (-R, 0)\ ;\ w_{1,1} = 1\ ;\ \mathbf{B}_{2,1} = (-(2+\sqrt{2})R/4, \sqrt{2}R/4)\ ;\ w_{2,1} = (2+\sqrt{2})/4 \\
\mathbf{B}_{3,1} = (-\sqrt{2}R/4, (2+\sqrt{2})R/4)\ ;\ w_{3,1} = (2+\sqrt{2})/4\ ;\ \mathbf{B}_{4,1} = (0, R)\ ;\ w_{4,1} = 1 \\
\mathbf{B}_{1,2} = (-(L+R)/2, 0)\ ;\ w_{1,2} = 1\ ;\ \mathbf{B}_{2,2} = (-(2+\sqrt{2})(L+R)/8, \sqrt{2}(L+R)/8)\ ;\ w_{2,2} = (2+\sqrt{2})/4 \\
\mathbf{B}_{3,2} = (-\sqrt{2}(L+R)/8, (2+\sqrt{2})(L+R)/8)\ ;\ w_{3,2} = (2+\sqrt{2})/4\ ;\ \mathbf{B}_{4,2} = (0, (L+R)/2)\ ;\ w_{4,2} = 1 \\
\mathbf{B}_{1,3} = (-L, 0)\ ;\ w_{1,3} = 1\ ;\ \mathbf{B}_{2,3} = \mathbf{B}_{3,3} = (-L, L)\ ;\ w_{2,3} = w_{3,3} = 1\ ;\ \mathbf{B}_{4,3} = (0, L)\ ;\ w_{4,3} = 1
\end{gathered} \tag{49}$$

The geometry and boundary conditions are given in Fig. 41. We assume a plane stress behavior, and specific boundary conditions are prescribed.

The considered damage law involves a delay effect in order to circumvent numerical issues

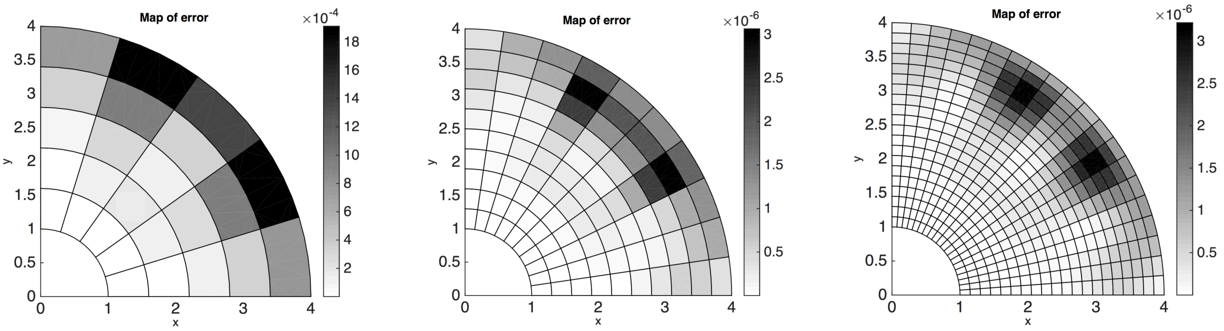

Figure 30: Map of the CRE estimate for the 5×5, 10×10, and 20×20 meshes (from left to right) and $p = 4$.

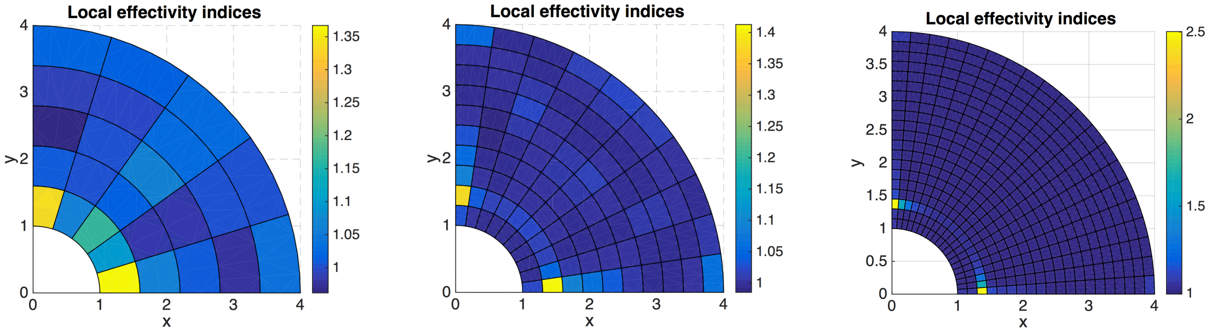

Figure 31: Map of local effectivity indices for the 5×5, 10×10, and 20×20 meshes (from left to right) and $p = 4$.

due to localization phenomena and mesh dependency. Such a model, described in [3, 57, 58], has been extensively used for composite materials. Following the general framework given in AppendixA, the material is split in two parts:

- state equations:

$$\begin{aligned} \sigma &= (1-d)\mathbf{K}_0\epsilon = \partial_\epsilon \psi^* \quad (0 \leq d \leq 1) \\ Y &= \frac{1}{2}\mathbf{K}_0\epsilon : \epsilon = \partial_d \psi \\ \beta &= (Y_c - Y_0)\alpha^2 = \omega(\alpha) = \partial_\alpha \psi \end{aligned} \tag{50}$$

  where d is the damage parameter, Y is the energy release rate, Y_0 is a threshold for damage appearing, Y_c is the critical threshold from which the material breaks, α is an additional internal variable, and β is the associated dual internal variable. The behavior law $\beta = \omega(\alpha)$, with $\omega(0) = 0$ and $\omega'(x) \geq 0$, takes an hardening effect into account. In this framework, the dissipation reads $Y\dot{d} - \beta\dot{\alpha}$, and potentials ψ and ψ^* are defined as:

$$\begin{aligned} \psi(\sigma, d, \alpha) &= \frac{1}{2}\frac{\mathbf{K}_0^{-1}\sigma : \sigma}{(1-d)} + \Psi_{d \leq 1} + Y_c\frac{|\alpha|^3}{3} \\ \psi^*(\epsilon, Y, \beta) &= Y + \Psi_{C_d}(\epsilon, Y) + \frac{2}{3}Y_c(\frac{|\beta|}{Y_c})^{3/2} \end{aligned} \tag{51}$$

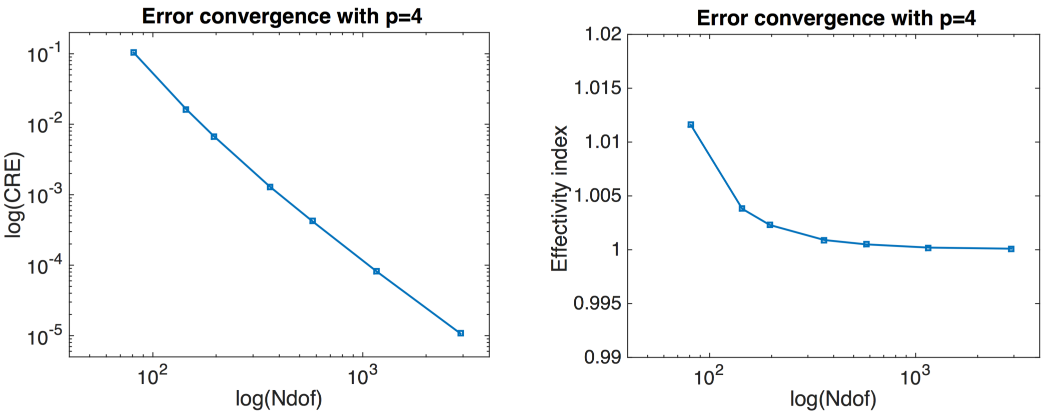

Figure 32: Convergence of the CRE estimate (left) and the global effectivity index (right) with respect to the number of dofs for $p = 4$.

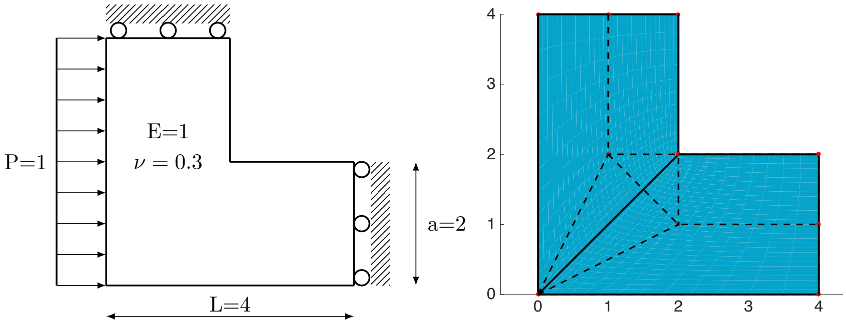

Figure 33: IGA representation of the L-shape geometry (left), and physical mesh (right).

where Ψ is the indicatrix function.

- evolution laws:

$$\begin{aligned} \dot{d} &= \frac{k}{a}\left(1 - exp(-a\langle\frac{Y - Y_0 - \beta}{Y_c - Y_0}\rangle_+)\right) = \partial_Y \varphi^* \\ -\dot{\alpha} &= -\dot{d} = \partial_\beta \varphi^* \\ d &= \alpha = 0 \quad \text{at } t = 0 \end{aligned} \tag{52}$$

The dissipation potential φ^* is defined as:

$$\begin{aligned} \varphi(\dot{d}, -\dot{\alpha}) &= \dot{d}\frac{(a-1)Y_0 + Y_c}{a} + (\frac{k}{a} - \dot{d})\ln(1 - \frac{a}{k}\dot{d}) \\ \varphi^*(Y, \beta) &= \frac{k}{a}\left[\langle Y - Y_0 - \beta\rangle_+ + \frac{Y_c - Y_0}{a}(exp(-\frac{a}{Y_c - Y_0}\langle Y - Y_0 - \beta\rangle_+) - 1)\right] \end{aligned} \tag{53}$$

As detailed in AppendixA, the residuals on state equations and evolution laws read,

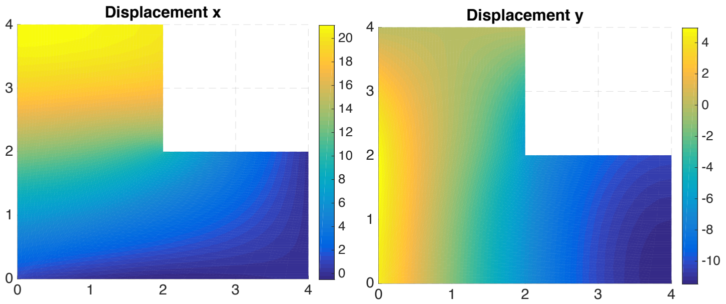

Figure 34: IGA displacement field $\mathbf{u}$, with components $\mathbf{u}\cdot\mathbf{e}_x$ (left) and $\mathbf{u}\cdot\mathbf{e}_y$ (right).

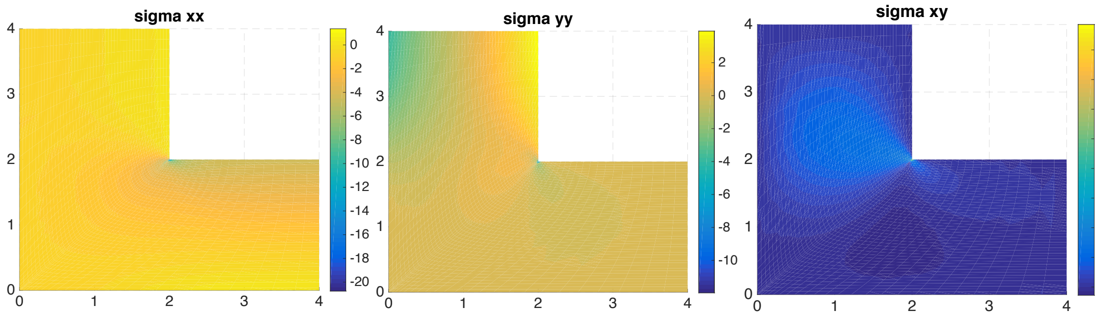

Figure 35: IGA stress field σ, with components σ_{xx} (left), σ_{yy} (center), and σ_{xy} (right).

respectively:

$$\begin{aligned}\eta_\psi(\epsilon, Y, \beta; \sigma, d, \alpha) &= \psi(\sigma, d, \alpha) + \psi^*(\epsilon, Y, \beta) - \sigma : \cdot\epsilon - Yd - \beta\alpha \geq 0 \\ \eta_\varphi(\dot{d}, -\dot{\alpha}; Y, \beta) &= \varphi(\dot{d}, -\dot{\alpha}) + \varphi^*(Y, \beta) - Y\dot{d} + \beta\dot{\alpha} \geq 0\end{aligned} \tag{54}$$

Remark 7. Gathering σ with variable d enables to obtain a convex potential $\psi(\sigma, d, \alpha)$. This would not be the case gathering ϵ with d as $\psi(\epsilon, d) = \frac{1}{2}\epsilon(1-d)\mathbf{K}_0\epsilon$ is not a convex function.

The problem is solved using a classical incremental procedure, with parameter values $E_0 = 6350$ (Young modulus), $Y_0 = 0$, $Y_c = 0.13$, $k = 7000$, and $a = 1$.The approximate damage fields at two different increments are represented in Fig. 41.

After computing an admissible set $\hat{\mathbf{\Sigma}}_h = (\hat{\epsilon}_h, \hat{Y}_h, \hat{\beta}_h, \hat{\sigma}_h, \hat{d}_h, \hat{\alpha}_h)$ from the approximate IGA solution, the CRE error estimate is defined as (see AppendixA):

$$E^2_{CRE}(\hat{\mathbf{\Sigma}}_h) = \int_\Omega \left[\eta_\psi\left(\hat{\mathbf{\Sigma}}_h\right) + \int_0^T \eta_\varphi\left(\hat{\mathbf{\Sigma}}_h\right)\mathrm{d}t\right]\mathrm{d}\mathbf{x} \tag{55}$$

In practice, the procedure to recover the admissible set $\hat{\mathbf{\Sigma}}_h$ follows that described in [57]; it uses the incremental solution of the problem, as well as the general procedure given in Section 4 for the recovery of an equilibrated stress field $\hat{\sigma}_h$. At each increment point k:

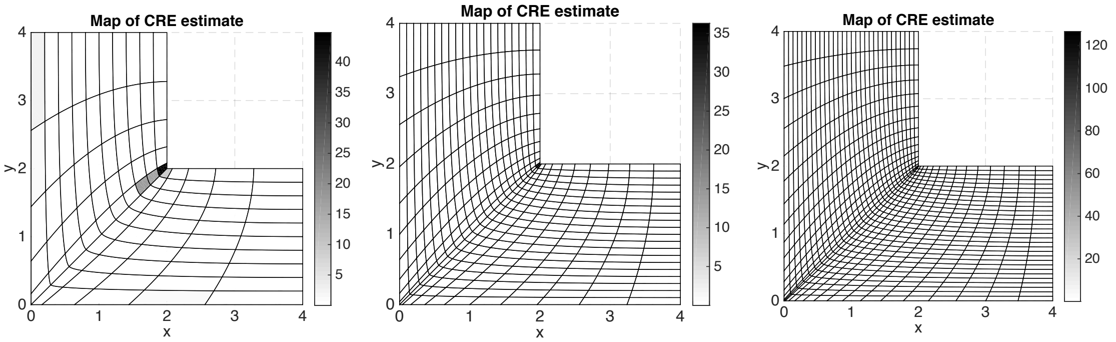

Figure 36: Map of the CRE error estimate for the L-shape domain and with various discretizations: 10 × 10 (left), 20 × 20 (center), and 30 × 30 (right) knot spans.

— we choose $\hat{\mathbf{u}}_h^{(k)} = \mathbf{u}_h^{(k)}$, i.e. $\hat{\epsilon}_h^{(k)} = \epsilon_h^{(k)}$;

— we construct $\hat{\sigma}_h^{(k)}$ from a post-processing of $\sigma_h^{(k)}$ using the procedure described in Section 4.

A linear interpolation between increment points is then performed to define fields $\hat{\epsilon}_h$ and $\hat{\sigma}_h$ over the whole time-space domain. Eventually, admissible internal variables $\hat{Y}_h$, $\hat{\beta}_h$, $\hat{d}_h$, and $\hat{\alpha}_h$ are chosen in order to minimize the CRE estimate. This constrained minimization procedure is cheap as it is performed locally at each integration point, and incrementally in time considering piecewise linear evolutions.

The obtained admissible stress field (at step 7) is represented in Fig. 42, whereas the spatial map of the CRE estimate (in terms of error density, as local contributions to the CRE estimate are normalized by the element size) as well as its evolution with step increments are given in Fig. 43. We observe that the CRE estimate increases with time, which is mechanically sound as damage grows in the same time. As for the normalized (relative) CRE estimate, it remains almost constant over the time domain. Here again, the results obtained from the CRE error estimate are consistent, with larger error in the vicinity of the damage zone and boundary conditions, and are useful indication for quantitative error assessment and mesh refinement.

6. Conclusions and prospects

In this work, we presented a general procedure based on the CRE framework for the computation of *a posteriori* error estimates for IGA simulations of linear or nonlinear structural mechanics models. It was shown that the main technical point, which is the construction of equilibrated flux/stress fields, could be performed from an extension of the hybrid-flux technique classically employed in the FEA context. This technique was thus extended from classical C^0-continuous Lagrange polynomials to C^k-continuous ($k > 0$) B-splines and NURBS bases. Numerical results confirmed the performance and potential of the approach, with effectivity indices above but very close to 1. It was mainly implemented on linear models, but it was also illustrated on a nonlinear damage model in order to show preliminary results

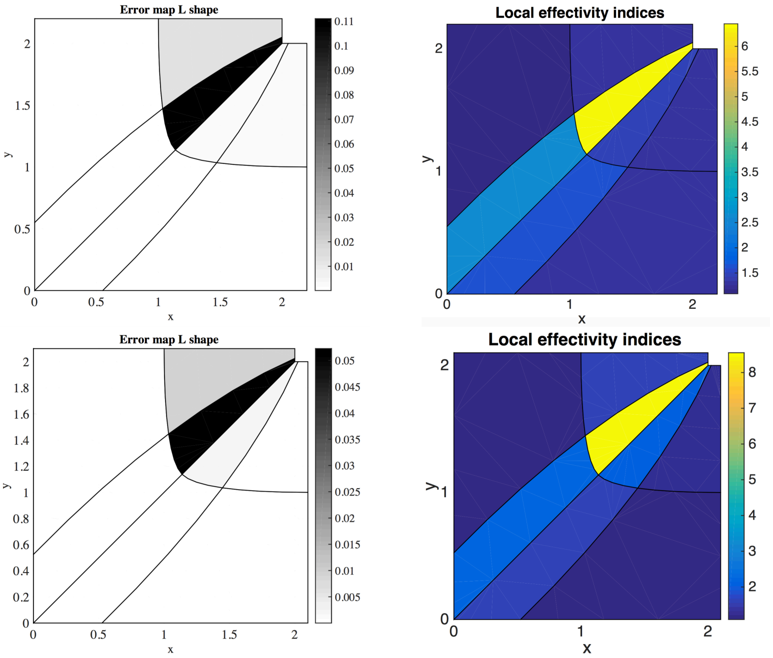

Figure 37: Map of the CRE error estimate (left) and local effectivity indices (right) for the L-shape domain, with two levels of graded meshes: Case 1 (top), Case 2 (bottom).

and some further potentialities of the approach. Consequently, the proposed work constitutes a practical tool for engineers aiming at controlling and adapting IGA computations efficiently. Forthcoming works will concentrate on the following points: (1) full analysis of the CRE estimate on complex nonlinear models such as damage models used for composite materials, for which IGA was shown to tremendously improve the design and analysis in recent works [27]; (2) goal-oriented error estimation using the CRE concept for nonlinear problems solved with IGA; (3) optimization of the constructed admissible fields when considering highly graded meshes; (4) implementation of the CRE error estimate into commercial software; (5) related to the previous point, potential combination of the approach with the facilitating Bézier extraction technology developed in [11, 77], in order to directly reuse hybrid-flux procedures implemented for FEA; (6) application with local refinement strategies based on recent technologies such as T-splines.

AppendixA. CRE functional for nonlinear material behaviors

From its original definition for linear thermal or elasticity problems [54], several formulations of the CRE concept have been proposed over the years in the case of nonlinear behaviors [59]. We focus here on the one described in [57, 58], which applies to the large class of material behaviors with standard formulation (such as (visco-)plasticity), and which is suited to material behaviors with softening.

The starting point is the formulation of the nonlinear material behavior in terms of state equations and evolution laws [39, 42]. Using the thermodynamical framework, we introduce

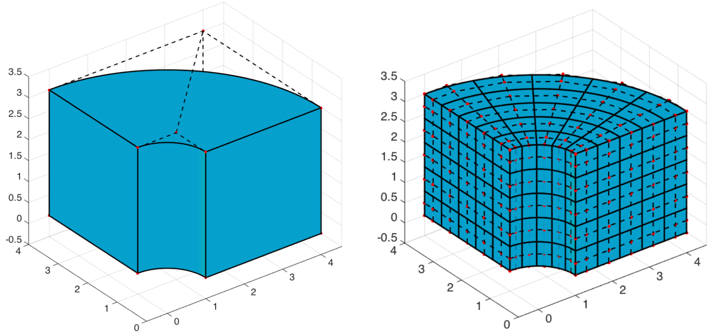

Figure 38: IGA representation of the 3D geometry.

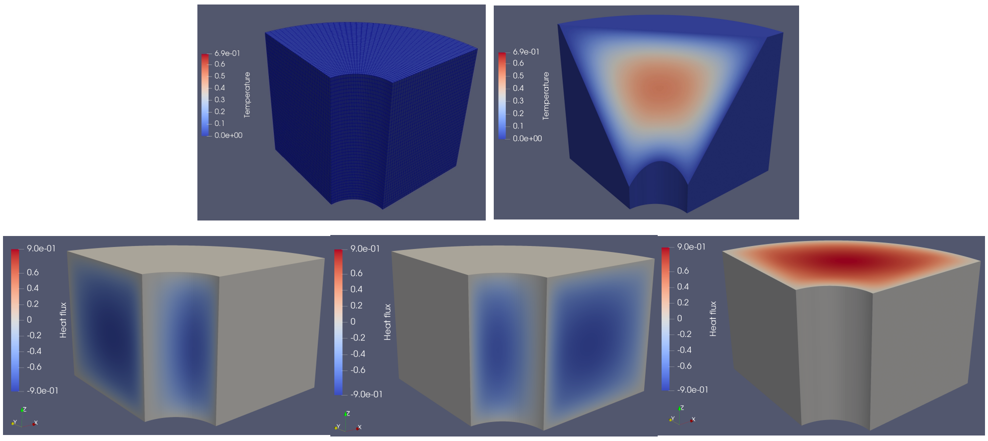

Figure 39: Approximate IGA solution: temperature (left), flux (right).

the Helmholtz free energy potential ψ:

$$\psi := \psi(T, \boldsymbol{\varepsilon}, \boldsymbol{\varepsilon}_p, \mathbf{V}) = \psi(T, \boldsymbol{\varepsilon}_e, \mathbf{V}) \tag{A.1}$$

that depends on state variables, i.e. observable variables (temperature T and strain tensor $\boldsymbol{\varepsilon}$) and internal variables: (i) the inelastic part $\boldsymbol{\varepsilon}_p$ of the strain tensor, such that $\boldsymbol{\varepsilon} = \boldsymbol{\varepsilon}_e + \boldsymbol{\varepsilon}_p$; (ii) additional internal variables V_i gathered in a vector $\mathbf{V}$. Then, the two first principles of thermodynamics lead to the Clausius-Duhem inequality (A.2):

$$\left(\boldsymbol{\sigma} - \rho \frac{\partial \psi}{\partial \boldsymbol{\varepsilon}_e}\right) : \dot{\boldsymbol{\varepsilon}}_e - \rho \left(s + \frac{\partial \psi}{\partial T}\right) \dot{T} - \sum_i \rho \frac{\partial \psi}{\partial V_i} \circ \dot{V}_i + \boldsymbol{\sigma} : \dot{\boldsymbol{\varepsilon}}_p - \frac{\mathbf{q} \cdot \nabla T}{T} \geq 0 \tag{A.2}$$

where ρ is the density, s is the entropy, and $\mathbf{q}$ is the thermal flux. Consequently, considering particular non-dissipative transformations, the previous inequality yields:

$$\boldsymbol{\sigma} = \partial_{\boldsymbol{\varepsilon}_e} \rho \psi \quad ; \quad s = -\partial_T \psi \tag{A.3}$$

Similarly, we can introduce thermodynamical loads Y_i (gathered in a vector $\mathbf{Y}$) associated with internal variables V_i:

$$Y_i = \partial_{V_i} \psi \tag{A.4}$$

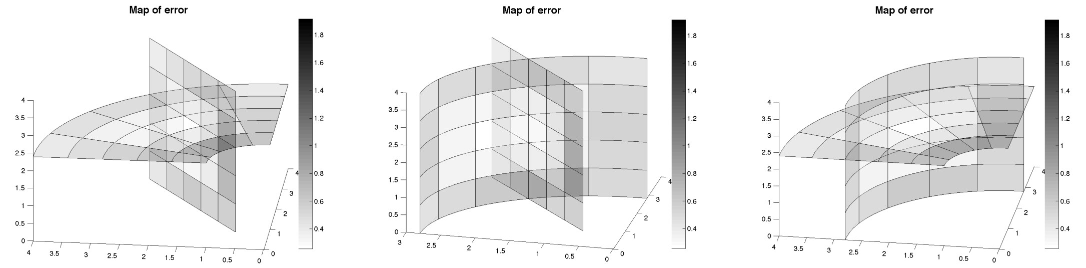

Figure 40: Map of the CRE estimate.

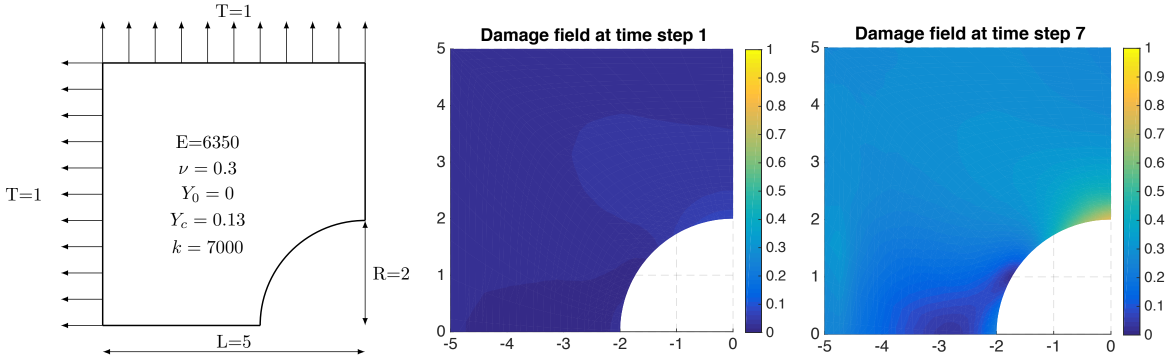

Figure 41: The considered problem (left), and approximate damage fields at increasing increments (center and right).

so that (A.2) can be recast in the following condensed format:

$$\boldsymbol{\sigma} : \dot{\boldsymbol{\varepsilon}}_p - \mathbf{Y} \cdot \dot{\mathbf{V}} - \frac{\mathbf{q} \cdot \nabla T}{T} \geq 0 \tag{A.5}$$

We mention that (A.3) and (A.4) constitute the state equations of the material behavior.

Remark 8. By duality, we can define the Gibbs free energy potential, denoted $\psi^\star$, as the Legendre-Fenchel transform of the Helmholtz free energy (A.1):

$$\psi^\star (T, \boldsymbol{\sigma}, \mathbf{Y}) = \sup_{\boldsymbol{\varepsilon}_e, \mathbf{V}} \left(\boldsymbol{\sigma} : \boldsymbol{\varepsilon}_e + \mathbf{Y} \cdot \mathbf{V} - \psi (T, \boldsymbol{\varepsilon}_e, \mathbf{V}) \right) \tag{A.6}$$

so that $\psi (T, \boldsymbol{\varepsilon}_e, \mathbf{V}) + \psi^\star (T, \boldsymbol{\sigma}, \mathbf{Y}) - \boldsymbol{\sigma} : \boldsymbol{\varepsilon}_e - \mathbf{Y} \cdot \mathbf{V} \geq 0$.

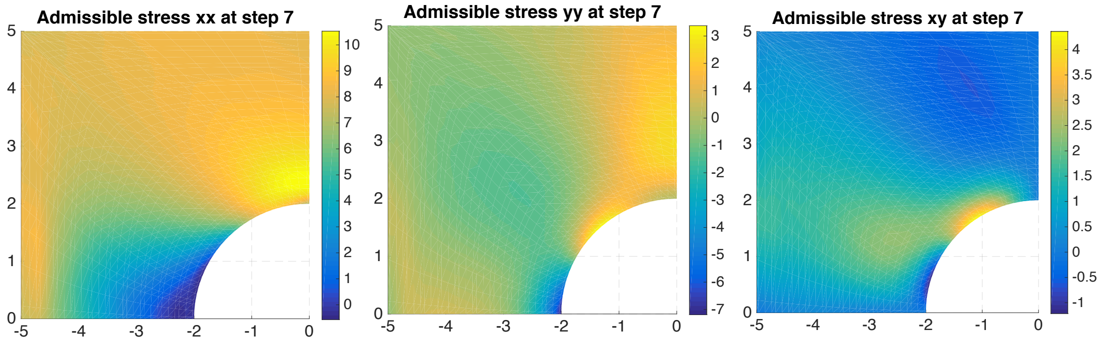

Figure 42: Admissible stress field: σ_{xx} (left), σ_{yy} (center), and σ_{xy} (right).

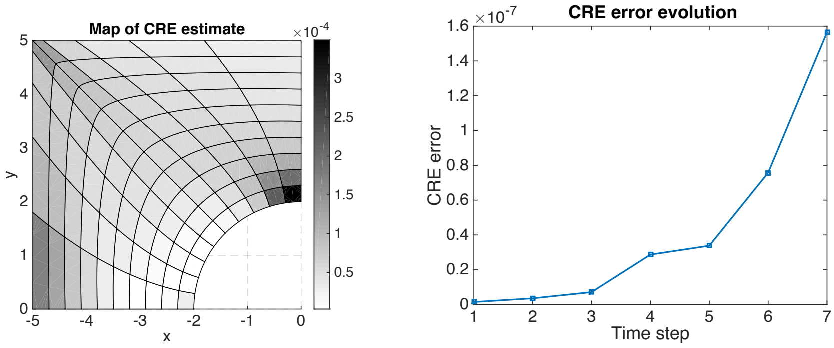

Figure 43: Map of the CRE estimate (left) and evolution with step increments (right).

Then, it can be shown using convex analysis [66] that state equations can be equivalently recast as:

$$\psi\left(T, \boldsymbol{\varepsilon}_e, \mathbf{V}\right) + \psi^\star\left(T, \boldsymbol{\sigma}, \mathbf{Y}\right) - \left\langle \left(\boldsymbol{\sigma}, \mathbf{Y}\right), \left(\boldsymbol{\varepsilon}_e, \mathbf{V}\right) \right\rangle = 0 \tag{A.7}$$

where we introduced the notation $\left\langle \left(\boldsymbol{\sigma}, \mathbf{Y}\right), \left(\boldsymbol{\varepsilon}_e, \mathbf{V}\right) \right\rangle = \boldsymbol{\sigma} : \boldsymbol{\varepsilon}_e + \mathbf{Y} \cdot \mathbf{V}$.

The inequality (A.5) reflects the dissipative evolution phenomena associated with the nonlinear material behavior. In particular, it imposes a consistency condition on the pair of variables $((\boldsymbol{\varepsilon}_p, \mathbf{V}), (\boldsymbol{\sigma}, \mathbf{Y}))$ in order to ensure that the intrinsic part $\boldsymbol{\sigma} : \dot{\boldsymbol{\varepsilon}}_p - \mathbf{Y} \cdot \dot{\mathbf{V}}$ of the dissipation remains positive. To satisfy the previous condition, it is usual and convenient to introduce a dissipation pseudo-potential, denoted $\varphi(\dot{\boldsymbol{\varepsilon}}_p, -\dot{\mathbf{V}})$, as well as its dual potential (defined using the Legendre-Fenchel transform):

$$\varphi^\star(\boldsymbol{\sigma}, \mathbf{Y}) = \sup_{\dot{\boldsymbol{\varepsilon}}_p, \dot{\mathbf{V}}} \left(\left\langle \left(\boldsymbol{\sigma}, \mathbf{Y}\right), \left(\dot{\boldsymbol{\varepsilon}}_p, -\dot{\mathbf{V}}\right) \right\rangle - \varphi(\dot{\boldsymbol{\varepsilon}}_p, -\dot{\mathbf{V}}) \right) \tag{A.8}$$

Then, evolution laws are defined from the gradients of potential φ (or $\varphi^\star$), involving an operator $\mathcal{B}$:

$$\begin{bmatrix} -\dot{\mathbf{V}} \\ \dot{\boldsymbol{\varepsilon}}_p \end{bmatrix} = \mathcal{B}\left(\begin{bmatrix} \mathbf{Y} \\ \boldsymbol{\sigma} \end{bmatrix} \right) = \partial_{(\boldsymbol{\sigma}, \mathbf{Y})} \varphi^\star(\boldsymbol{\sigma}, \mathbf{Y}) \tag{A.9}$$

so that the Clausius-Duhem inequality (A.5), which comes down to positive definite properties of the operator $\mathcal{B}$:

$$\begin{bmatrix}\mathbf{Y}\\ \boldsymbol{\sigma}\end{bmatrix} \cdot \mathcal{B}\left(\begin{bmatrix}\mathbf{Y}\\ \boldsymbol{\sigma}\end{bmatrix}\right) \geq 0 \tag{A.10}$$

is naturally satisfied when dissipation pseudo-potentials are chosen convex, with $\varphi(\mathbf{0},\mathbf{0}) = \varphi^*(\mathbf{0},\mathbf{0}) = 0$.

From the previous thermodynamical formulation of nonlinear behaviors, a general CRE measure was derived in [57] from residuals on: (i) the state equations; (ii) the evolution laws. These residuals are defined using the Legendre-Fenchel inequality applied to the corresponding thermodynamical potentials. They read:

— residual on the state equations:

$$\eta_\psi(\boldsymbol{\varepsilon}_e, \mathbf{V}, \boldsymbol{\sigma}, \mathbf{Y}) = \psi(\boldsymbol{\varepsilon}_e, \mathbf{V}) + \psi^\star(\boldsymbol{\sigma}, \mathbf{Y}) - \langle(\boldsymbol{\sigma}, \mathbf{Y}), (\boldsymbol{\varepsilon}_e, \mathbf{V})\rangle \geq 0 \tag{A.11}$$

— residual on the evolution laws:

$$\eta_\varphi(\dot{\boldsymbol{\varepsilon}}_p, -\dot{\mathbf{V}}, \boldsymbol{\sigma}, \mathbf{Y}) = \varphi(\dot{\boldsymbol{\varepsilon}}_p, -\dot{\mathbf{V}}) + \varphi^\star(\boldsymbol{\sigma}, \mathbf{Y}) - \left\langle(\boldsymbol{\sigma}, \mathbf{Y}), (\dot{\boldsymbol{\varepsilon}}_p, -\dot{\mathbf{V}})\right\rangle \geq 0 \tag{A.12}$$

We notice again that convex analysis yields $\eta_\psi = 0$ (resp. $\eta_\varphi = 0$) when state equations (resp. evolution laws) are satisfied.

For the sake of simplicity, we denote $\boldsymbol{\Sigma} = (\boldsymbol{\varepsilon}_e, \boldsymbol{\varepsilon}_p, \mathbf{V}, \boldsymbol{\sigma}, \mathbf{Y})$ the whole set of variables. From the two residuals (A.11,A.12), the local in space and time CRE measure e_{CRE} is defined as:

$$e^2_{CRE}(\boldsymbol{\Sigma}) = \eta_\psi(\boldsymbol{\Sigma}) + \int_0^t \eta_\varphi(\boldsymbol{\Sigma})\,\mathrm{d}t \quad \forall \mathbf{x} \in \Omega, \forall t \in I_t \tag{A.13}$$

and a global measure can be obtained by integration over the space-time domain.

[1] Ainsworth M, Oden J.T. A posteriori error estimation in finite element analysis. *Vol. 37, Wiley-Interscience, New York* 2000.

[2] Allier P.E, Chamoin L, Ladevèze P. Towards simplified and optimized a posteriori error estimation using PGD reduced models. *International Journal for Numerical Methods in Engineering* 2018; **113(6)**:967–998.

[3] Allix O, Deu J.F. Delayed-damage modelling for fracture prediction of laminated composites under dynamic loading. *Engineering Transactions* 1997; **45**:29–46.

[4] Auricchio F, Beirao da Veiga L, Hughes T.J.R, Reali A, Sangalli G. A simple algorithm for obtaining nearly optimal quadrature rules for NURBS-based isogeometric analyis. *Computer Methods in Applied Mechanics and Engineering* 2012; **249-252**:15–27.

[5] Babuska I, Strouboulis T, Upadhyay C.S, Gangaraj S.K, Copps K. Validation of a posteriori error estimators by numerical approach. *International Journal for Numerical Methods in Engineering* 1994; **37**(7):1073–1123.

[6] Bank R.E, Smith R.K. A posteriori error estimates based on hierarchical bases. *SIAM Journal of Numerical Analysis* 1993; **30**(4):921–935.

[7] Bazilevs Y, Beirao da Veiga L, Cottrell J.A, Hughes T.J.R, Sangalli G. Isogeometric analysis: approximation, stability and error estimates for h-refined meshes. *Mathematical models and Methods in Applied Sciences* 2006; **16**(7):1031–1090.

[8] Bazilevs Y, Calo V.M, Hughes T.J.R, Zhang Y. Isogeometric fluid-structure interaction: theory, algorithms, and computations. *Computational Mechanics* 2008; **43**:3–37.

[9] Beirao da Veiga L, Buffa A, Rivas J, Sangalli G. Some estimates for h-p-k refinement in isogeometric analysis. *Numerische Mathematik* 2011; **118**(2):271–305.

[10] Benson D.J, Bazilevs Y, Hsu M.C, Hughes T.J.R. Isogeometric shell analysis: the Reissner-Mindlin Shell. *Computer Methods in Applied Mechanics and Engineering* 2010; **199**:276–289.

[11] Borden M, Scott M, Evans J, Hughes T.J.R. Isogeometric finite element data structures based on Bezier extraction of NURBS. *International Journal for Numerical Methods in Engineering* 2011; **87**(1-5):15–47.

[12] Bouclier R, Elguedj T, Combescure A. An isogeometric locking-free NURBS-based solid-shell element for geometrically nonlinear analysis. *International Journal for Numerical Methods in Engineering* 2014; **101**:774–808.

[13] Braess D, Pillwein V, Schöberl J. Equilibrated residual error estimates are p-robust. *Computer Methods in Applied Mechanics and Engineering* 2009; **198**:1189–1197.

[14] Buffa A, Sangalli G, Vazquez R. Isogeometric analysis in electromagnetics: B-spline approximation. *Computer Methods in Applied Mechanics and Engineering* 2010; **199**(17-20):1143–1152.

[15] Buffa A, Giannelli C. Adaptive isogeometric methods with hierarchical splines: error estimator and convergence. *Mathematical Models and Methods in Applied Sciences* 2016; **26**(1):1–25.

[16] Buffa A, Garau E.M. A posteriori error estimators for hierarchical B-spline discretizations. *Mathematical Models and Methods in Applied Sciences* 2018; **28**(8):1453–1480.

[17] Chamoin L, Ladevèze P. Bounds on history-dependent or independent local quantities in viscoelasticity problems solved by approximate methods. *International Journal for Numerical Methods in Engineering* 2007; **71**(12):1387–1411.

[18] Chamoin L, Ladevèze P. A non-intrusive method for the calculation of strict and efficient bounds of calculated outputs of interest in linear viscoelasticity problems. *Computer Methods in Applied Mechanics and Engineering* 2008; **197**(9-12):994–1014.

[19] Chamoin L, Diez P. Verifying calculations, forty years on: an overview of classical verification techniques for FEM simulations. *SpringerBriefs* 2015.

[20] Chemin A, Elguedj T, Gravouil A. Isogeometric local h-refinement strategy based on multigrids. *Finite Elements in Analysis and Design* 2015; **100**(C):77–90.

[21] Cottereau R, Diez P, Huerta A. Strict error bounds for linear solid mechanics problems using a subdomain-based flux-free method. *Computational Mechanics* 2009; **44**(4):533–547.

[22] Cottrell J.A, Reali A, Bazilevs Y, Hughes T.J.R. Isogeometric analysis of structural vibrations. *Computer Methods in Applied Mechanics and Engineering* 2006; **195**(41-43):5257–5296.

[23] Cottrell J.A, Hughes T.J.R, Bazilevs Y. Isogeometric analysis: towards integration of CAD and FEA. *John Wiley & Sons, Chichester, UK* 2009.

[24] Dalcin L, Collier N, Vignal P, Cartes A.M.A, Calo V.M. PetIGA: a framework for high-performance isogeometric analysis. *Computer Methods in Applied Mechanics and Engineering* 2016; **308**:151–181.

[25] De Lorenzis L, Wriggers P, Zavarise G. A mortar formulation for 3D large deformation contact using NURBS-based isogeometric analysis and the augmented Lagrangian method. *Computational Mechanics* 2012; **49**(1):1–20.

[26] Deng J, Chen F, Li X, Hu C, Tong W, Yang Z, Feng Y. Polynomial splines over hierarchical T-meshes. *Graphical Models* 2008; **70**:76–86.

[27] Deng X, Korobenko A, Yan J, Bazilevs Y. Isogeometric analysis for continuum damage in rotation-free composite shells. *Computer Methods in Applied Mechanics and Engineering* 2015; **284**:349–372.

[28] Destuynder P, Métivet B. Explicit error bounds in a conforming finite element method. *Mathematics of Computation* 1999; **68**(288):1379–1396.

[29] Dorfel M, Juttler B, Simeon B. Adaptive isogeometric analysis by local h-refinement with T-splines. *Computer Methods in Applied Mechanics and Engineering* 2010; **199**(5-8):264–275.

[30] Dufour J-E, Antolin P, Sangalli G, Auricchio F, Reali A. A cost-effective isogeometric approach for composite plates based on a stress recovery procedure. *Computer Methods in Applied Mechanics and*

Engineering 2010; **199**(5-8):264–275.

[31] Elguedj T, Bazilevs Y, Calo V.M, Hughes T.J.R. $\bar{B}$ and $\bar{F}$ projection methods for nearly incompressible linear and nonlinear elasticity and plasticity using higher-order NURBS elements. *Computer Methods in Applied Mechanics and Engineering* 2008; **197**(33-40):2732–2762.

[32] Ern A, Vohralik M. A posteriori error estimation based on potential and flux reconstruction for the heat equation. *SIAM Journal on Numerical Analysis* 2010; **345**(48):198–223.

[33] Evans J.A, Bazilevs Y, Babuska I, Hughes T.J.R. n-Widths, sup-infs, and optimality ratios for the k-version of the isogeometric finite element method. *Computer Methods in Applied Mechanics and Engineering* 2009; **198**(21-26):1726–1741.

[34] Feischl M, Gantner G, Praetorius D. Reliable and efficient a posteriori error estimation for adaptive IGA boundary element methods for weakly-singular integral equations. *Computer Methods in Applied Mechanics and Engineering* 2015; **290**:362–386.

[35] Florentin E, Gallimard L, Pelle J-P. Evaluation of the local quality of stresses in 3d finite element analysis. *Computer Methods in Applied Mechanics and Engineering* 2002; **191**:4441–4457.

[36] Forsey D, Bartels R. Hierarchical B-spline refinement. *Computer Graphics* 1988; **22**(4):205–212.

[37] Fraeijs de Veubeke B. Displacement and equilibrium models in the finite element method. *International Journal for Numerical Methods in Engineering, Classical Reprint Series* 2001; **52**:287–342.

[38] Gallimard L. A constitutive relation error estimator based on traction-free recovery of the equilibrated stress. *International Journal for Numerical Methods in Engineering* 2009; **78**(4):460–482.

[39] Germain P, Nguyen Q.S, Suquet P. Continuum thermodynamics. *Journal of Applied Mechanics* 1983; **50**:1010–1020.

[40] Giannelli C, Juttler B, Speleers H. THB-splines: the truncated basis for hierarchical splines. *Computer Aided Geometric Design* 2012; **29**(7):485–498.

[41] Gomez H, Calo V.M, Bazilevs Y, Hughes T.J.R. Isogeometric analysis of the Cahn-Hilliard phase-field model. *Computer Methods in Applied Mechanics and Engineering* 2008; **197**:4333–4352.

[42] Halphen B, Nguyen Q.S. Sur les matériaux standard généralisés. *Journal de mécanique* 1975; **14**:39–63.

[43] Höllig K. Finite Element Methods with B-Splines. *SIAM, Philadelphia* 2003.

[44] Hosseini S, Remmers J, Verhoosel C, De Borst R. Propagation of delamination in composite materials with isogeometric continuum shell elements. *International Journal for Numerical Methods in Engineering* 2015; **102**:159–179.

[45] Hughes T.J.R, Cottrell J.A, Bazilevs Y. Isogeometric analysis: CAD, finite elements, NURBS, exact geometry and mesh refinement. *Computer Methods in Applied Mechanics and Engineering* 2005; **194**:4135–4195.

[46] Hughes T.J.R, Reali A, Sangalli G. Efficient quadrature for NURBS-based isogeometric analysis. *Computer Methods in Applied Mechanics and Engineering* 2010; **199**(5-8):301–313.

[47] Johannessen K.A, Kvamsdal T, Dokken T. Isogeometric analysis using LR B-splines. *Computer Methods in Applied Mechanics and Engineering* 2014; **269**:471–514.

[48] Kagan P, Fischer A, Bar-Yoseph P.Z. New B-spline finite element approach for geometrical design and mechanical analysis. *International Journal for Numerical Methods in Engineering* 1998; **41**:435–458.

[49] Kiendl J, Bletzinger KU, Linhard J, Wchner R. Isogeometric shell analysis with Kirchhoff-Love elements. *Computer Methods in Applied Mechanics and Engineering* 2009; **198**(49-52):3902–3914.

[50] Kleiss S.K, Tomar S.K. Guaranteed and sharp a posteriori error estimates in isogeometric analysis. *Computers & Mathematics with Applications* 2015; **70**(3):167–190.

[51] Kruse R, Nguyen-Thanh N, De Lorenzis L, Hughes T.J.R. Isogeometric collocation for large deformation elasticity and frictional contact problems. *Computer Methods in Applied Mechanics and Engineering* 2015; **296**:73–112.

[52] Kumar M, Kvamsdal T, Johannessen K.A. Superconvergent patch recovery and a posteriori error estimation technique in adaptive isogeometric analysis. *Computer Methods in Applied Mechanics and Engineering* 2017; **316**:1086–1156.

[53] Kuru G, Verhoosel C.V, Van der Zee K, Van Brummelen E.H. Goal-adaptive isogeometric analysis with hierarchical splines. *Computer Methods in Applied Mechanics and Engineering* 2014; **270**:270–292.

[54] Ladevèze P, Leguillon D. Error estimate procedure in the finite element method and application. *SIAM Journal of Numerical Analysis* 1983; **20**(3):485–509.

[55] Ladevèze P, Maunder E.A.W. A general method for recovering equilibrating element tractions. *Computer Methods in Applied Mechanics and Engineering* 1996; **137**:111–151.

[56] Ladevèze P, Rougeot P. New advances on a posteriori error on constitutive relation in finite element analysis. *Computer Methods in Applied Mechanics and Engineering* 1997; **150**:239–249.

[57] Ladevèze P, Moes N, Douchin B. Constitutive relation error estimators for (visco)plastic finite element analysis with softening. *Computer Methods in Applied Mechanics and Engineering* 1999; **176**:247–264.

[58] Ladevèze P. Constitutive relation error estimations for finite element analyses considering (visco)-plasticity and damage. *International Journal for Numerical Methods in Engineering* 2001; **52**(5-6):527–542.

[59] Ladevèze P, Pelle J.P. Mastering Calculations in Linear and Nonlinear Mechanics. *Springer, New York* 2004.

[60] Ladevèze P. Strict upper error bounds on computed outputs of interest in computational structural mechanics. *Computational Mechanics* 2008; **42**(2):271–286.

[61] Ladevèze P, Chamoin L. Calculation of strict error bounds for finite element approximations of non-linear pointwise quantities of interest. *International Journal for Numerical Methods in Engineering* 2010; **84**(13):1638–1664.

[62] Ladevèze P, Chamoin L. The constitutive relation error method: a general verification tool. Verifying calculations, forty years on: an overview of classical verification techniques for FEM simulations. *SpringerBriefs* 2015; 59–94.

[63] Lipton S, Evans J.A, Bazilevs Y, Elguedj T, Hughes T.J.R. Robustness of isogeometric structural discretizations under severe mesh distortion. *Computer Methods in Applied Mechanics and Engineering* 2010; **199**:357–373.

[64] Machiels L, Maday Y, Patera A. A flux-free nodal Neumann subproblem approach to output bounds for partial differential equations. *Comptes Rendus Académie des Sciences - Mécanique, Paris* 2000; **330**(1):249–254.

[65] Moitinho de Almeida J.P, Maunder E.A.W. Equilibrium Finite Element Formulations. *Wiley* 2017.

[66] Moreau J.J. Convexity and duality. *Functional Analysis and Optimization, Academic Press, New-York* 1996:145–169.

[67] Nguyen-Xuan H, Hoang T, Nguyen V.P. An isogeometric analysis for elliptic homogenization problems. *Computers and Mathematics with Applications* 2014; **67**:1722–1741.

[68] Paraschivoiu M, Peraire J, Patera A.T. A posteriori finite element bounds for linear-functional outputs of elliptic partial differential equations. *Computer Methods in Applied Mechanics and Engineering* 1997; **150**(1-4):289–312.

[69] Pares N, Diez P, Huerta A. Subdomain-based flux-free a posteriori error estimators. *Computer Methods in Applied Mechanics and Engineering* 2006; **195**(4-6):297–323.

[70] Piegl L, Tiller W. The NURBS Book (Monographs in Visual Communication). *Second Edition, Springer-Verlag, New York* 1997.

[71] Pled F, Chamoin L, Ladevèze P. On the techniques for constructing admissible stress fields in model verification: Performances on engineering examples. *International Journal for Numerical Methods in Engineering* 2011; **88**(5):409–441.

[72] Pled F, Chamoin L, Ladevèze P. An enhanced method with local energy minimization for the robust a posteriori construction of equilibrated stress fields in finite element analyses. *Computational Mechanics* 2012; **49**:357–378.

[73] Prudhomme S, Oden J.T. On goal-oriented error estimation for elliptic problems: application to the control of pointwise errors. *Computer Methods in Applied Mechanics and Engineering* 1999; **176**(1-4):313–331.

[74] Rey V, Gosselet P, Rey C. Study of the strong prolongation equation for the construction of statically admissible stress fields: implementation and optimization *Computer Methods in Applied Mechanics and Engineering* 2014; **268**:82–104.

[75] Schillinger D, Dedè L, Scott M, Evans J, Borden M, Rank E, Hughes T. An isogeometric design-through-analysis methodology based on adaptive hierarchical refinement of NURBS, immersed boundary methods, and T-spline CAD surfaces. *Computer Methods in Applied Mechanics and Engineering* 2012; **249-252**:116–150.

[76] Schillinger D, Evans J, Reali A, Scott M, Hughes T. Isogeometric collocation: Cost comparison with Galerkin methods and extension to adaptive hierarchical NURBS discretizations. *Computer Methods in Applied Mechanics and Engineering* 2013; **267**:170–232.

[77] Schillinger D, Ruthala P.K, Nguyen L.H. Lagrange extraction and projection for NURBS basis functions: a direct link between isogeometric and standard nodal finite element formulations. *International Journal for Numerical Methods in Engineering* 2016; **108(6)**:515–534.

[78] Sederberg T.W, Cardon D.L, Finnigan G.T, North N.S. T-spline simplification and local refinement. *ACM Transactions on Graphics* 2004; **23**(3):276–283.

[79] Sevilla R, Fernandez-Mendez S, Huerta A. 3D NURBS-enhanced finite element method (NEFEM). *International Journal for Numerical Methods in Engineering* 2011; **88**:103–125.

[80] Temizer I, Wriggers P, Hughes T. Contact treatment in isogeometric analysis with NURBS. *Computer Methods in Applied Mechanics and Engineering* 2011; **200**:1100–1112.

[81] Verfurth R. A review of a posteriori error estimation and adaptive mesh refinement techniques. *Wiley-Teubner, Stuttgart* 1996.

[82] Vuong A.V, Giannelli C, Juttler B, Simeon B. A hierarchical approach to adaptive local refinement in isogeometric analysis. *Computer Methods in Applied Mechanics and Engineering* 2011; **200**:3554–3567.

[83] Waeytens J, Chamoin L, Ladevèze P. Guaranteed error bounds on pointwise quantities of interest for transient viscodynamics problems. *Computational Mechanics* 2012; **49**(3):291–307.

[84] Wall W.A, Frenzel M.A, Cyron C. Isogeometric structural shape optimization. *Computer Methods in Applied Mechanics and Engineering* 2008; **197**(33-40):2976–2988.

[85] Xu G, Mourrain B, Duvigneau R, Galligo A. A new error assessment method in isogeometric analysis of 2D heat conduction problems. *Advanced Science Letters* 2012; **10**(1):508–512.